March 12, 2026

Evidence for holocentric centromeres in the early branching apicomplexan parasite *Cryptosporidium parvum*

Running title: Holocentricity in *Cryptosporidium*

Abigail Kimball[1#], Wanyi Huang[1#], Rui Xu[1,a], Melanie Key[1], Lisa Funkhouser-Jones[1,b], and L. David Sibley[1*]

[#] Contributed equally

Department of Molecular Microbiology, Washington University School of Medicine, St. Louis, MO 63110, USA

Present addresses:

[a] State Key Laboratory for Animal Disease Control and Prevention, South China Agricultural University, Guangzhou 510642, China

[b] Department of Microbial Pathogenesis & Immunology, Naresh K. Vashisht School of Medicine, Texas A&M University, Bryan, TX 77807, USA

*Address correspondence to Dr. L. David Sibley, Department of Molecular Microbiology, Washington University School of Medicine, 660 S. Euclid, CB 8230 St. Louis MO 63110. E-mail address: sibley@wustl.edu

Keywords: apicomplexan, mitosis, centromeres, holocentric, *Cryptosporidium*

ABSTRACT (150 limit)

During its asexual cycle, *Cryptosporidium parvum* (*C. parvum*) amplifies through three rounds of nuclear division before undergoing cytokinesis to form infectious merozoites. However, chromosome organization and segregation during nuclear division remain unstudied. Here, we visualized H3-histones, including the centromeric histone H3 (CENH3), telomeres, and centrosomes during mitosis. Nuclear division was accompanied by centrosome duplication and elongated microtubules that spanned the dividing nuclei. Surprisingly, *C. parvum* centromeres detected by CENH3 showed diffuse staining throughout nuclear division, that overlapped with telomeres in the apical nucleus. Analysis of centromeres based on CENH3 capture and DNA sequencing revealed numerous distinct binding sites scattered across all eight chromosomes, including both coding regions and intergenic regions, that were typified by GA rich repeat sequences. The unique holocentric chromosome structure of *C. parvum* is unlike the single regional centromeres found in related apicomplexans, suggesting it arose independently from other known examples in plants, insects and worms.

INTRODUCTION

Cryptosporidium parvum (C. parvum), an obligate intracellular parasite, remains a serious global health and agricultural threat [1-4]. Transmission occurs through the ingestion of infectious oocysts and causes severe diarrheal illness in infants, young animals, and immunocompromised adults [5-7]. Once ingested, sporozoites exit the oocyst, invade host cells, and undergo three rounds of nuclear division within a single shared cytoplasm (the process of merogony), followed by cytokinesis to produce eight identical merozoites. Newly formed merozoites are released into the lumen, where they invade new host cells, and repeat the

47 invasion-egress cycle three times before transitioning to the sexual phase of the life cycle [8, 9].
48 Despite its significance as a global health problem, and the novelty of apicomplexan nuclear
49 division processes, *C. parvum* mitosis remains largely uncharacterized, with our current
50 understanding limited to basic microscopy studies [8, 10-15].

51 To divide rapidly, apicomplexans appear to rely on several features that are thought to
52 streamline nuclear division. Comparative cell biology suggests that maintaining chromosomes in
53 a minimally condensed state may reduce the need for extensive chromatin remodeling during
54 division, although the extent to which this directly accelerates mitosis remains to be fully
55 resolved [16, 17]. This adaptation necessitates strict nuclear organization during mitosis, where
56 centromeres are typically maintained on the apical end of the nucleus attached to the
57 centrosomes, and telomeres persistently cluster at the basal end of the nuclear periphery [18-20].
58 Additionally, apicomplexans maintain their nuclear envelope throughout mitosis, minimizing the
59 energy and time required for breakdown and reformation [17, 21]. A consequence of this closed
60 mitosis is restricted access of spindle fibers to chromosomes, necessitating alternative
61 segregation mechanisms based on intranuclear spindles. Rather than centrosomes orchestrating
62 microtubule organization from the cytoplasm, apicomplexan centrosomes (spindle pole bodies,
63 microtubule-organizing centers) are embedded within the nuclear envelope and serve as spindle
64 assembly hubs that elongate the microtubules so they can attach to the centromeres and
65 ultimately coordinate chromosome movement during division [22-29]. It has been postulated that
66 nuclear pores are essential for nucleocytoplasmic transport through the intact envelope and
67 directly support the process of spindle assembly [30, 31]. Electron microscopy studies suggest
68 that *C. parvum* undergoes schizogony, with multiple rounds of nuclear replication preceding a
69 cytoplasmic division, followed by the egress of daughter parasites from the host cell [13].

70 During mitosis and meiosis, centromeres function to orchestrate chromosome segregation
71 by serving as sites for microtubule anchoring to assure faithful separation at metaphase [32].
72 Centromeres have variable architecture in different organisms consisting of point centromeres
73 (small 250 bp single site per chromosome) in yeast [33], regional centromeres (gene poor islands
74 of heterochromatin ranging from several to hundreds of kb) in *T. gondii* and *P. falciparum* [26,
75 27, 34], and holocentric chromosomes (multiple centromere sites along the chromosome) found
76 in multiple species of plants, insects and worms [35-37]. Although centromere function is
77 essential and highly conserved across eukaryotes, centromeric DNA sequences and size are
78 subject to rapid evolution [38-40]. Variation in centromere architecture affects nuclear
79 organization, karyotype changes, and ultimately drives speciation [41, 42].
80 The nuclear structures, chromosome features, and mitotic mechanisms, including the role of
81 centromeres, have not been examined previously in *C. parvum*. Here, we delineate the
82 fundamental biology of *C. parvum* mitosis, revealing significant deviations from previously
83 assumed mechanisms. Using high-resolution imaging we examined nuclear division during the
84 first round of merogony, leveraging multiple transgenic parasite strains and mitosis-specific
85 antibodies. Additionally, we used Cleavage Under Targets and Nuclease Release (CUT&RUN)
86 [43] to identify the location of the centromeres based on CENH3 and patterns of centromere-
87 associated histone modifications in *C. parvum* and the related parasite *Toxoplasma gondii* (*T.*
88 *gondii*). In contrast to the monocentric centromeric structure of *T. gondii*, we found that *C.*
89 *parvum* has a dispersed centromeric chromosome structure with CENH3 binding sites scattered
90 across multiple small regions on all 8 chromosomes, resulting in diffuse CENH3 centromere
91 staining throughout mitosis. Overall, these results suggest that *C. parvum* employs a divergent

92 mitotic mechanism compared to other well-studied apicomplexans and has convergently evolved
93 holocentric architecture.
94
95 **RESULTS**
96 ***Characterization of centromeric histone H3 (CENH3) and histone H3 candidates in C.***
97 ***parvum***
98 The genome annotation of *C. parvum* contains two genes encoding Histone H3 *cgd3_2540* and
99 *cgd4_3220* (referred to here as H3.1 and H3.2, respectively) and a third gene *cgd4_2030*
100 annotated as a centromere-specific Histone H3 variant (CENH3). To validate these annotations,
101 we performed multiple BLASTP analyses using the protein products of each of these three *C.*
102 *parvum* genes to identify top hits in the following groups: 1) Apicomplexa (excluding all
103 *Cryptosporidium* species), 2) all eukaryotic organisms (excluding all Apicomplexa), 3) *Homo*
104 *sapiens*, and 4) *Saccharomyces cerevisiae.* Collectively, these analyses provide strong support
105 for cgd4_2030 as the CENH3 ortholog in *C. parvum* (**Table 1**). To examine the relationship
106 between the protein sequences for the *C. parvum* genes of interest and the top hits of BLASTP
107 analyses, a phylogenetic tree was generated (**Fig 1A**). We found that *cgd3_2540* (H3.1) and
108 *cgd4_3220* (H3.2) closely cluster with histone H3 sequences from other organisms, whereas
109 *cgd4_2030* (CENH3) clustered with other centromeric histone H3 proteins. We then directly
110 compared the amino acid sequences of H3.1 and H3.2 with a global sequence alignment and
111 found that the two sequences were highly similar (99.26%), but less similar compared to the
112 CENH3 (65.10% and 64.43%, respectively) (**Table 2 and Fig 1B**).

113 **Table 1:** The results of BLASTP analyses using the *C. parvum* centromeric histone H3-like protein (*cgd4_2030*), histone H3-like

114 proteins (*cgd3_2540* and *cgd4_3220).*

115

116 *

Query	Top hits in Apicomplexa*	E value	Top hits in all Eukaryotes#	E value	Top hits in *Saccharomyces cerevisiae*	E value	Top hits in *Homo sapiens*	E value
cgd4_2030 (CENH3)	histone H3-like centromeric protein CSE4 [*C. cionae*]	5e-46	centromeric DNA-binding histone H3-like protein cse4 [*N. ribis*]	3e-39	Chain A, Cse4	2e-30	Chain A, Histone H3.1, Histone H3-like centromeric protein A, Histone H3.1	5e-39
cgd3_2540 (H3.1)	histone H3 [*C. cionae*]	2e-86	histone H3-like [*P. hypophthalmus*]	3e-86	histone H3	4e-81	histone H3.2	1e-88
cgd4_3220 (H3.2)	histone H3 [*C. cionae*]	2e-90	histone H3-like [*P. hypophthalmus*]	2e-87	histone H3	2e-81	histone H3.2	1e-89

117 *C.*

118 *parvum* proteins were compared against all organisms in the Apicomplexa phylum (except for *Cryptosporidium* spp.),

119 # *C. parvum* proteins were compared against all organisms (except for Apicomplexa)

120

121

122 **Table 2:** The identity and similarity results from multiple global sequence alignments between

123 H3.1, H3.2, and CENH3 proteins using a BLOSUM62 scoring matrix.

***Cp* H3.1 and *Cp* H3.2**	***Cp* CENH3 and *Cp* H3.1**	***Cp* CENH3 and *Cp* H3.2**
	Identity: 46.31% Similarity: 65.10% Gaps: 14.09%	
Identity: 97.78% Similarity: 99.26% Gaps: 0.00%		Identity: 46.31% Similarity: 64.43% Gaps: 14.09%

124

125 To further explore the distribution of H3.1 and H3.2 H3 variants, we generated two

126 transgenic lines of parasites that replaced the dispensable thymidine kinase (*tk*) gene with a

127 second copy of *cgd3_2540* (referred to as H3.1-3HA) or *cgd4_3220* (referred to as H3.2-3HA)

128 fused with a triple hemagglutinin (3HA) epitope tag using CRISPR/Cas9 (**Fig 1C, S1 A-B Fig,**

129 **Table S1**). Transgenic parasites were used to infect a human adenocarcinoma cell line (HCT-8)

130 monolayer, cultures were fixed at 18 hours post infection (hpi) during merogony, stained, and the

131 localization of the 3HA tag was observed by immunofluorescence (IFA) high-resolution

132 confocal laser scanning microscopy equipped with Airyscan detection (LSCM-A). We found that

133 H3.1-3HA (**Fig 1D**) and H3.2-3HA (**Fig 1E**) had a diffuse staining pattern, which was expected

134 based on histone H3 staining in other apicomplexan parasites [27, 44, 45]

135

136 ***The staining pattern of C. parvum centromeric histone H3 (CENH3) is distinct.***

137 To visualize *C. parvum* centromeres, we used CRISPR-Cas9 gene editing to add a 3HA tag to

138 the C-terminus of the centromere-specific histone H3 variant protein (referred to as CENH3-

139 3HA) (**Fig 2A, S3 A-B Fig, Table S1**). After successfully selecting and amplifying these

140 transgenic parasites in immunocompromised mice, we infected HCT-8 cells for 22 h and

141 examined the staining pattern by LSCM-A microscopy. For these studies, we chose mature
142 meronts that were oriented with the basal side of the vacuole at the surface of the host cell where
143 it attaches at the feeder organelle and where the majority of meronts were projecting upward, as
144 ascertained by fluorescence staining and Z-stack images running perpendicular from bottom to
145 top of the parasite (see cartoon on **Fig 3C**). The CENH3 staining pattern observed in *C. parvum*
146 was unexpectedly highly diffuse and occupied the apical half of the nucleus (**Fig 2B-C**) in
147 contrast to the more dispersed pattern found in the H3.1-3HA and H3.2-3HA tagged parasites
148 (**Fig 1 D,E**). The diffuse pattern of CENH3 staining in *C. parvum* contrasts sharply with the
149 focal pattern of regional centromeres previously described in *T. gondii* [27, 46]. Hence, we
150 utilized a CENH3-3HA-tagged *T. gondii*, gifted by Dr. Kami Kim, as a staining control for our
151 experiments. These parasites were used for the infection of HCT-8 cells, fixed at 24 hpi, stained,
152 and examined by high-resolution LSCM-A immunofluorescence (IFA) microscopy (**Fig 2D-E)**.
153 We found that the staining pattern of the centromeric histone H3 in *T. gondii* is punctate, similar
154 to what has been found previously in *T. gondii* by other investigators [27, 46].
155
156 ***Distribution of centrosomes in C. parvum.***
157 A vital step in mitosis is centrosome duplication, and previous studies in apicomplexans have
158 shown that it can be traced using antibodies that recognize the centrin 1 protein [27, 47]. A single
159 point adjacent to the nucleus occurs in non-replicating cells, while two centrin 1 positive points
160 per nucleus indicates the parasite is undergoing replication [27, 47]. In *Plasmodium*, during
161 schizogony, asynchronous duplications of centriolar plaques, centrosomes, have been observed
162 across multiple nuclei within a single cytoplasm, in this study we sought to identify analogous
163 centrosomes in *C. parvum*. [28]. To identify parasites undergoing early mitosis, we infected

164 HCT-8 cells with excysted wild type *C. parvum* sporozoites, washed off uninvaded sporozoites
165 at 2 h, fixed the cultures at various timepoints between 6.5-8.5 hpi, and stained with Hoechst and
166 an anti-centrin-1 antibody. Initially, trophozoites contained a single centrin-1 focus associated
167 with the single nucleus (**S4A**). However, in other examples of trophozoites, we often observed
168 that each nucleus consistently exhibited two centrin-1 positive points (**Fig 2F**). Furthermore, by
169 visualizing the number of nuclei based on Hoechst staining, and centrin-1 to monitor dividing
170 centrosomes, we observed that all nuclei found in a common cytoplasm shared the same centrin-
171 1 staining pattern. For example, when 2N or 4N meronts were observed to have duplicated the
172 centriole as shown by centrin-1 staining, the duplicated pattern was consistently observed for all
173 nuclei within that cell (**Fig 2F**). To determine if the diffuse centromere staining pattern persisted
174 during active mitosis in *C. parvum*, we infected cultures with CENH3-3HA parasites and
175 repeated the experiment previously described. We found that nuclei undergoing mitosis also
176 displayed a diffuse CENH3-3HA staining pattern by LSCM-A (**Fig 2G**). We also attempted to
177 localize CENH3 using ultrastructure expansion or immuno-EM staining methods. Despite
178 extensive troubleshooting, we could not identify positive signals in N- or C-terminally tagged
179 CENH3-3HA lines, or in separate line expressing a spaghetti monster (sm)HA tag (i.e. CENH3-
180 smHA), by either method, which may be due to the low abundance of CENH3 or difficulty
181 preserving the epitope during these procedures.
182
183 ***The telomere (G-strand binding protein, GBP) staining pattern is apical in C. parvum.***
184 Previous studies in *Plasmodium* have found that the telomeres are consistently found on the
185 opposite pole to the centromeres [48-50]. Since the centromeres were located toward the apical
186 end of the nuclei in meronts, we expected that *C. parvum* telomeres would be more basal. To

187 examine the distribution of telomere in *C. parvum*, we utilized a surrogate protein marker. G-
188 quadruplex structures readily form at repetitive telomeric sequences and require G-quadruplex
189 binding proteins (GBPs) for stabilization (**Fig 3A**). A previous study identified *cgd1_3530* as the
190 GBP in *C. parvum* and determined the specific sequence necessary for *Cp*GBP binding
191 (GGTTA) [51]. Using AlphaFold and ChimeraX, we modeled the G-quadruplex structure
192 formed by this repetitive sequence and visualized how the *Cp*GBP protein interacts with and
193 stabilizes it. (**Fig 3B**). To identify the location of *C. parvum* telomeres relative to the
194 centromeres, we engineered transgenic parasites to express a 3HA tag at the gene encoding the
195 C-terminus of the G-quadruplex binding protein (referred to as GBP-3HA) (**Fig 3C, S3 A-B Fig,**
196 **Table S1**). LSCM-A microscopy on infected HCT-8 monolayers (24 hpi) revealed that the
197 telomeres were located toward the apical side of the nucleus (**Fig 3D**), rather than at the opposite
198 pole as expected.
199
200 ***The telomere (GBP) and centromere (CENH3) staining patterns overlap in C. parvum.***
201 To confirm that *C. parvum* centromeres and telomeres had overlapping nuclear locations, we
202 generated an additional line of transgenic parasites that replaced the dispensable thymidine
203 kinase (*tk*) gene with a second copy of an N-terminally 3HA tagged CENH3 and GBP C-
204 terminally tagged with 3Ty via CRISPR/Cas9, with an intervening P2A split peptide to facilitate
205 co-expression of separate proteins (referred to as 3HA-CENH3-GBP-Ty) (**Fig 3E, S1C-D Fig,**
206 **Table S1)**. HCT-8 cultures were infected with 3HA-CENH3-GBP-Ty parasites, fixed at 6.5 hpi,
207 and examined by LSCM-A microscopy after staining. We observed that 3HA-CENH3 and
208 GBP-3Ty signals were both more concentrated in the apical region of the nucleus, as defined by
209 Hoechst staining. This overlap was evident by fluorescence microscopy and further supported

210 quantitatively using the Coloc2 plugin in FIJI/ImageJ, which yielded a Pearson correlation
211 coefficient of 0.96 (**Fig 3F, S2 Fig)**.
212
213 ***Detection of mitotically active DNA, microtubules, and the nuclear pore proteins in C. parvum***
214 The phosphorylation of histone H3 (specifically at serine 10 and serine 28) is a highly conserved
215 mechanism for initiating chromosome condensation in preparation for mitosis [52]. Antibodies
216 recognizing the phosphorylated version of H3 at serine 10 are commonly used in other systems
217 to determine which cells are currently undergoing mitosis from late interphase through telophase
218 [53]. Even though apicomplexan parasites are known not to condense their chromosomes, *C.*
219 *parvum* meronts frequently stained positive for the phosphorylated histone H3 (PH3) antibody
220 (**Fig 4A**), suggesting they are in the process of mitosis. Previous studies have characterized the
221 distribution of nuclear pores in *Plasmodium falciparum* using a rabbit polyclonal antibody to the
222 protein NUP116 [54]. We rationalized that the epitope recognized by this antibody might also be
223 conserved in *C. parvum*, despite their evolutionary distance. We visualized nuclear pores in *C.*
224 *parvum* using the rabbit anti- NUP116 antibody and found that it reliably stained the parasite
225 nucleus in a punctate pattern that was concentrated primarily peripherally in the nucleus (**Fig**
226 **4B**). Although we have not verified the identity of this cross-reaction, it presumably represents a
227 component of nuclear pores that will be used for future studies on nuclear organization in *C.*
228 *parvum.*
229 Among apicomplexan parasites, mitosis has primarily been studied in *T. gondii* and *P.*
230 *falciparum* [16, 17, 27, 55]. These prior studies demonstrate that once centrosomes duplicate,
231 and the nuclear envelope forms a tunnel-like structure, organizing spindle microtubules within it,
232 spindle microtubules then attach at the centromere and mediate chromosome movement [56]. We

233 also attempted to visualize this process in *C. parvum* by staining with antibodies that recognize
234 the centrin-1 nd alpha tubulin (**Fig 4C-D, S4B-C**). We examined cells at 6-7 hpi to capture early
235 stages of mitosis. We frequently observed two conformations of centrin-1 tubulin structures that
236 may represent early (**Fig 4C, S4B**) and late mitotic phases (**Fig 4D, S4C**). In Fig 4C, the
237 duplicated centrin signal shows a single discrete spindle (microtubule signal) overlying
238 what appears to be a single nucleus, as evident by size and shape. In other examples the
239 centrin spots have moved further away, and the spindles elongated (Y-shaped) (**Fig 4D,**
240 **S4C**). Notably, the nucleus in this image is much larger and diffuse, consistent with it
241 being at a later stage that is starting to divide.
242
243 ***Composition of centromeres in C. parvum and T. gondii***
244 Centromeres are defined by the deposition of CENH3-containing nucleosomes [27, 57]. Given
245 the diffuse staining of CENH3, we wanted to further characterize the centromere by identifying
246 DNA sites bound by this protein. Therefore, we adopted protocols for CUT&RUN to identify
247 centromeres based on CENH3 binding based on capture with anti-HA antibody in *C. parvum*
248 [43]. To ensure sufficient HA binding, we developed a CENH3 line tagged with spaghetti
249 monster (referred to as CENH3-smHA) that contains 10 HA epitope repeats for these
250 experiments and validated identical staining patterns to CENH3-3HA *C. parvum* (**S3 A-C Fig,**
251 **Table S1**). To validate our experimental strategy, we first applied CUT&RUN to *T. gondii*,
252 whose centromeres have previously been defined by ChIP-seq [27]. Our CUT&RUN data
253 closely matched earlier findings, with CENH3 enrichment observed at discrete chromosomal loci
254 corresponding to the previously described centromeres (**Fig 5A, S5A-C Fig**). We also detected
255 the positive correlation of CENH3 with H3K9me3 and inverse correlation with H3K4me3

256 reported in earlier ChIP-chip analyses (**Fig 5A, S5A-B Fig**). Based on these signals, we
257 implemented a stepwise strategy to identify centromeric regions. Valleys in H3K4me3,
258 consisting of 20 kb windows, sized to match reported centromere lengths (16 kb ± 3.4 kb)[27],
259 combined with co-enrichment of H3K9me3 with CENH3-smHA were used as criteria for
260 identifying centromere regions (**S5D Fig**). Applying these rules, we identified a single
261 centromere in each of the 13 chromosomes of *T. gondii* (**S5E Fig**), with Chr VIIb identified as
262 part of Chr VIII [58](**S5C Fig**).
263 We next applied CUT&RUN to *C. parvum*. Initial experiments using a 120-minute MNase
264 digestion failed to generate usable data, as both sequencing depth and genome coverage were
265 low compared to negative controls (**S1 Dataset**). Since CENH3 nucleosomes can be
266 hypersensitive to MNase digestion, as reported previously in *Caenorhabditis elegans* (*C.*
267 *elegans)* [57], we tested digestion times of 5, 30, and 60 min. The 30 min digestion yielded the
268 best coverage and sequencing depth, and these conditions were used for following analyses (**S1**
269 **Dataset, S6A Fig**). Notably, sequencing depth of the *C. parvum* samples was more variable and,
270 in some cases, lower than that of *T. gondii*. This difference primarily reflects technical
271 challenges associated with generating transgenic *C. parvum* parasites. To ensure data quality and
272 comparability, we included only samples with high genome coverage (>80%) in downstream
273 analyses. Unlike *T. gondii*, read mapping profiles for CENH3 in *C. parvum* showed signals
274 broadly distributed along chromosomes (**Fig 5B**). To locate centromeric regions in *C. parvum*,
275 we first attempted the *T. gondii* stepwise strategy, but no valid windows were detected. As the
276 CENH3 distribution resembled that of the holocentric nematode *C. elegans*, we adjusted
277 thresholds accordingly by restricting the peaks analysis to 400 bp windows (**S6B Fig**). We
278 identified 423 CENH3-enriched regions distributed across all chromosomes. Heatmaps and

279 aggregate signal profiles showed that these windows displayed features of CENH3 enrichment
280 correlated with H3K9me3 deposition and H3K4me3 depletion, suggesting that they represent
281 centromere-associated chromatin (**S6C-D Fig**). Importantly, these signals were largely absent in
282 wild type parasites stained with HA antibody as a control, supporting their authenticity (**S6C-D**
283 **Fig**). To further refine localization, we excluded windows overlapping with WT-HA signals,
284 reducing the dataset to 347 high-confidence centromeric windows (**S6B,E Fig**). Taken together,
285 these results indicate that *C. parvum* possesses many small CENH3 binding sites dispersed
286 across eight chromosomes, in contrast to the monocentric nature of *T. gondii*.
287 We further investigated characteristics of *C. parvum* centromeres. In contrast to *T. gondii*,
288 where centromeres are typically located within large intergenic regions [27], no extended
289 intergenic regions were observed in *C. parvum* due to the tight compaction of the genome.
290 Surprisingly, the majority of *C. parvum* CENH3-associated windows were located within gene
291 coding regions rather than being restricted to intergenic regions (**S2 DataSet2**). To evaluate
292 evolutionary constraints on CENH3-associated regions, we performed nucleotide diversity (Pi)
293 analyses on the DNA sequences within these regions and dN/dS analyses on the genes
294 overlapping these windows. We compared previously generated genomic sequences from
295 numerous *C. parvum* IIa and IId isolates, which show high genomic similarity. Most CENH3-
296 associated windows (~82%) showed reduced Pi values compared with genome-wide 400-bp
297 sliding windows, and only a single gene within the windows exhibited an elevated dN/dS ratio
298 relative to the genome-wide orthologous gene set (**S6F,G Fig**). These results indicate that
299 CENH3-associated regions are highly conserved and under strong purifying selection. To
300 determine whether centromeric regions were also present within intergenic regions of *C. parvum*,
301 we applied a stepwise identification strategy using a slightly relaxed read depth threshold (**S6F**

302 **Fig**). We identified 58 centromeric regions distributed within intergenic regions across all
303 chromosomes (**Fig. 5C, S3 DataSet**). Heatmaps and aggregate signal profiles for CNEH3 as well
304 as chromatin marks also supported that they represent centromere-associated chromatin (**Fig.**
305 **5D,E**). These results suggest that CENH3 binding in *C. parvum* is broadly distributed throughout
306 the chromosomes, including both with in coding regions and intergenic regions. To assess
307 sequence properties of *C. parvum* centromeric windows, motif analysis of *C. parvum*
308 centromeric windows was performed using MEME, revealing two GA-rich motifs enriched at
309 CENH3-associated sites (**Fig 5F**). Notable, these GA repeats are also found in other regions of
310 the genome that were not identified in the CENH3 capture studies.
311
312
313 **DISCUSSION**
314 Despite rapid asexual proliferation being required for parasite expansion, the molecular
315 mechanisms that underlie *C. parvum* mitosis have remained unexplored. To investigate this
316 process, we examined nuclear division using markers to track multiple rounds of mitosis during
317 merogony. Nuclear division in *C. parvum* can be visualized by staining with phospho-H3 and
318 centrin-1, which provide markers for mitotically active chromatin and duplicating centrosomes,
319 respectively. Surprisingly, both CENH3, a marker for centromeres, and GBP, a marker for
320 telomeres, were diffusely localized across the apical half of the nucleus. Moreover, these diffuse
321 apical patterns persisted throughout mitosis, as shown by visualizing nuclear division stages with
322 centrin-1 and microtubules. To explore the molecular nature of centromeres, we performed
323 CUT&RUN sequencing of transgenic parasites expressing epitope-tagged CENH3. Although
324 discrete monocentric peaks were detected in the related parasite *T. gondii*, CENH3 binding sites

325 were diffusely scattered across ~ >400 sites in the *C. parvum* genome. Overall, these findings
326 indicate that *C. parvum* has evolved an alternative chromosome structure compared to other
327 apicomplexan parasites, differences that may have significant functional consequences for
328 chromosome stability and meiotic recombination.

329 Following entry of sporozoites (or merozoites) into the host cell, the parasite undergoes
330 merogony, consisting of 3 rounds of nuclear division prior to cytokinesis to generate infectious
331 merozoites. By visualizing the number of nuclei based on Hoechst staining, and centrin-1 to
332 monitor dividing centrosomes, we observed that all nuclei found in a common cytoplasm shared
333 the same centrin-1 staining pattern (single centrin-1 spot when not dividing and duplicated
334 centrin-1 spot prior to nuclear division). This pattern suggests that nuclei within a single meront
335 may divide synchronously, although further studies using synchronized cells and live cell
336 imaging would be needed to substantiate this hypothesis. This pattern differs from *Plasmodium*
337 schizogony, where nuclei are observed at different mitotic stages within a single schizont [28]. In
338 *Plasmodium*, nuclear pores are important for division as they facilitate the transport of mitotic
339 molecules through the intact nuclear envelope and associate with the centriolar plaques [31, 59].
340 Although we did not examine the dynamics of nuclear pores during division, they appear as
341 peripheral puncta in mature meronts and may serve a similar function in *C. parvum*.

342 Staining with alpha-tubulin allowed us to visualize *C. parvum* microtubules during mitosis,
343 particularly at early stages where microtubules form a cluster that may represents the spindle that
344 will drive chromosome separation during mitosis. The pattern of microtubules described here in
345 dividing cels is quite different from the stable, elongate microtubules that emanate from the
346 apical pole of sporozoites and merozoites [60]. Such dramatic re-organization of microtubules
347 between non-dividing and dividing cells is not unusual for eukaryotic cells, although the

348 dynamics and regulation of this process have not been examined extensively in *Cryptosporidium*.
349 Based on qualitative observations of centrosome duplication, centrin-1 positioning, microtubule
350 organization, and changes in nuclear morphology, our studies suggest an approximate sequence
351 of events corresponding to sequential rounds of mitosis during early, mid, and late merogony.
352 Further studies using fluorescently tagged proteins and life cell imaging, combined with
353 synchronous cell division would be important to validate and extend this model. Regardless of
354 the exact dynamics of mitosis, these studies provide an important foundation for studies of the
355 dynamics of centromere staining described below.

356 Unexpectedly, we found a diffuse nuclear CENH3-3HA staining pattern rather than the
357 punctate pattern observed in other apicomplexan parasites [27, 29, 34]. We also confirmed that
358 the diffuse CENH3 staining pattern did not deviate when the method of tagging was altered (e.g.
359 smHA), when the location of the tag was swapped (N-terminally tagged, e.g. 3HA-CENH3-
360 GBP-3Ty), or when a tagged second copy of the gene was inserted into a neutral locus of the
361 genome (3HA-CENH3-GBP-3Ty). We also developed epitope-tagged lines of telomere-binding
362 protein GBP, similar to studies in *Eimeria* and *Plasmodium* [61, 62]. Unlike in other
363 apicomplexans, GBP was also localized to the apical half of the nucleus in *C. parvum*,
364 overlapping closely with CENH3 [18-20, 48]. We further confirmed that the telomeres and
365 centromeres occupied a similar nuclear location using a parasite strain in which CENH3 and
366 GBP proteins were simultaneously expressed as tagged second copies. This pattern contrasts
367 sharply with other apicomplexans where telomers are localized to the opposite pole of the
368 nucleus from centromeres [48-50]. We sought to determine if centromeres remained diffuse
369 throughout mitosis by simultaneously visualizing the centrosomes and centromeres by staining
370 CENH3-3HA with anti-HA and centrin-1 antibodies. We confirmed that in *C. parvum,* the

371 diffuse centromere staining pattern does not change throughout mitosis, which further contrasts
372 with the highly focal nature of centromeres in *T. gondii* and *P. falciparum* [26, 27].
373 Given the highly unusual staining patterns of CENH3 in *C. parvum*, we decided to
374 investigate CENH3 binding sites on DNA using CUT&RUN sequencing. For comparison, we
375 also performed CUT&RUN studies on CENH3 in the related parasite *T. gondii* and compared
376 them to previous studies that used ChIPSeq to define centromeres [27]. In *T. gondii*, CUT&RUN
377 sequencing identified highly similar CENH3 binding sites to those reported previously by
378 ChIPSeq [27] with a single predominant peak on each chromosome, including newly defined
379 peaks on chromosome IV, that had not been identified previously. Centromeres in *T. gondii*
380 consist of gene-poor regions of ~15 kb that are not defined by any particular sequence or repeats
381 but instead are positively correlated with H3K9me3 and inversely correlated with H3K4me3,
382 typical chromatin patterns expected for centromeric regions [18, 27]. Under similar conditions,
383 CUT&RUN experiments for CENH3 binding sites in *C. parvum* failed to identify similar
384 singular dominant peaks on each chromosome. Instead, CENH3 binding sites were
385 hypersensitive to MNase digestion, with the signal being the highest at a 30- min incubation
386 time, similar to that observed in ChIP-seq studies of the holocentric nematode *Caenorhabditis*
387 *elegans* (*C. elegans*) [57]. Under optimal digestive conditions, we found that the CENH3 signal
388 in *C. parvum* was broadly distributed along chromosomes, with ~ 350 distinct sites in coding
389 regions and another ~ 60 sites within intergenic regions scattered across 8 chromosomes.
390 Interestingly, like *T. gondii*, *C. parvum* CENH3 peaks also correlated with H3K9me3 signal and
391 were found in areas lacking H3K4me3, consistent with a centromere-associated chromatin
392 pattern. The distribution of CENH3 binding sites in *C. parvum* is similar to that described in *C.*

393 *elegans* as polycentric, implying that CENH3 binds to distinct sites rather than diffusely across
394 the entire chromosome [57].

395 Collectively, our findings are consistent with *C. parvum* containing holocentric centromeres
396 based on the following criteria: Firstly, the staining pattern of CENH3 diffusely stains the apical
397 half of the nucleus under nondividing conditions, in contrast to the focal staining of CENH3 in *T.*
398 *gondii* [18, 27] and *P. falciparum* [26]. Secondly, the diffuse pattern of CENH3 staining remains
399 throughout mitosis, suggesting centromeres do not coalesce into a single regional center. Thirdly,
400 CENH3 binding sites as defined by CUT&RUN resemble the dispersed pattern of low-intensity
401 peaks seen in *C. elegans*, which has well-characterized holocentric chromosomes. Although we
402 interpret this diffuse distribution as consistent with holocentric centromeres, we acknowledge
403 that an alternative explanation, such as asynchronous chromatid separation or cohesion fatigue,
404 could also contribute to the observed pattern. However, current imaging resolution does not
405 allow simultaneous visualization of all microtubules and all CENH3-associated kinetochore
406 sites, so we cannot fully distinguish between these possibilities. Therefore, we present our
407 interpretation cautiously while noting that the number of predicted CENH3 loci substantially
408 exceeds the 8 (1N) regional centromeres expected for a monocentric organization. Finally, the
409 CENH3 binding sites show evidence of simple GA nucleotide repeats, a feature also seen in *C.*
410 *elegan*s [57]. In both cases, the GA repeats are also found in other regions of the respective
411 genomes, so this feature alone is not sufficient to mediate CENH3 binding. One unusual feature
412 of the CENH3 binding sites in *C. parvum* is that they extend into coding regions, which is not an
413 expected feature of centromeres. Interestingly, these regions were under strong purifying
414 selection at the intraspecies level. The dispersed polycentric pattern of CENH3 binding sites in
415 *C. elegans* is also unusual in that these regions are concentrated in High Occupancy Targets

416 (HOT) sites for permissive binding of transcription factors [57]. In *C. elegans*, the CENH3 and
417 HOT sites appear to serve a dual purpose: in replicating cells they bind CENH3, while they
418 recruit transcription factors when CENH3 is lost during exit from the cell cycle in differentiated
419 muscle cells [57]. By analogy, transcriptional silencing during mitosis in *C. parvum* may allow
420 CENH3 binding in coding regions to facilitate chromatid segregation, with displacement during
421 the rest of the cell cycle when transcription is active. Alternatively, the CENH3 binding sites in
422 intergenic regions may function as the primary centromere-localizing signal for formation of
423 kinetochores.

424 Holocentric chromosomes have been documented in many species, primarily through direct
425 cytological observation, yet their functional implications and evolutionary origins remain poorly
426 understood [37, 57, 63, 64]. Recent comparative and modeling work in fungi shows that
427 complete transitions between centromere 'types' (point/regional/holocentric) occur progressively
428 and do not fix by drift alone; rather, selection is needed to drive and stabilize new architectures
429 while maintaining compatibility with the relatively conserved kinetochore–spindle interface [65].
430 In this light, *the* many small CENH3-binding sites in *C. parvum* fits a model of progressive
431 centromere remodeling along an evolutionary continuum, rather than representing an abrupt
432 departure from other apicomplexan centromere types.

433 The organization we describe has clear functional implications, as the presence of hundreds
434 of small CENH3-positive sites suggests that *C. parvum* chromosomes may rely on numerous
435 'micro-kinetochores' distributed along their length. By spreading spindle attachment across
436 many small units rather than concentrating mechanical force at a single centromere, the parasite
437 could effectively diffuse the load generated during chromosome segregation. Such a system
438 would be particularly advantageous for *C. parvum*, which performs closed mitosis with

439 uncondensed chromatin and must execute multiple rounds of synchronous division during rapid
440 merogony. In this framework, the diffuse, apically clustered distribution of CENH3 is not simply
441 a structural anomaly, but an evolved solution to the mechanical and cell-cycle constraints
442 imposed by rapid, multi-round division in an intestinal environment. Thus, the centromere
443 architecture of *C. parvum* likely reflects selective pressures associated with maintaining
444 chromosome stability, rather than a simple deviation from typical apicomplexan chromosome
445 biology.

446 Current evidence suggests that holocentric chromosomes have evolved convergently at least
447 13 times across distantly related taxa in both the plant and animal kingdoms [36, 37, 64].
448 Holocentricity has not previously been described in protists, and hence it likely evolved
449 convergently in *C. parvum*. However, we note that the directionality of centromere evolution
450 within Apicomplexa remains unresolved. Because centromere organization has not been
451 characterized in closely related outgroups such as gregarines or chromerids, it is equally
452 plausible that the common ancestor of Apicomplexa possessed holocentric chromosomes and
453 that monocentric organization arose secondarily in coccidia and hematozoa. Thus, the
454 holocentric architecture in *C. parvum* may represent either an independently derived state or the
455 retention of an ancestral condition. It is also possible that holocentricity is more widespread
456 among protists, but that it has been overlooked due to their small size and failure to condense
457 chromosomes during division.

458 One proposed advantage of holocentricity is its capacity to stabilize chromosomal fragments
459 during mitosis, thereby mitigating genetic loss. This trait may confer a selective benefit to
460 organisms frequently exposed to elevated levels of DNA damage due to environmental stressors
461 or lifestyle factors [36, 63]. Thus, holocentricity may impart genome stability under stress

462 encountered in the gastrointestinal system where the parasite is exposed to toxic bacterial
463 metabolites [66] and host immune responses [67]. Despite this potential advantage,
464 holocentricity also presents a major challenge for coordinating chromatid segregation following
465 crossover during meiosis I. Well-characterized holocentric species have evolved mechanisms to
466 circumvent this issue, such as inverted meiosis or, in the case of *C. elegans*, the deployment of
467 kinetochore proteins that localize to discrete chromosomal regions, effectively mimicking
468 monocentric behavior [68]. Whether *C. parvum* uses a similar mechanism as *C. elegans* to
469 localize kinetochore proteins to discrete sites on the chromosome is uncertain, but previous work
470 from our laboratory examining crossover rates during *C. parvum* meiosis revealed a high
471 frequency of crossover events and failed to find evidence for inverted meiosis, a process used by
472 some holocentric organisms [69]. In contrast, interspecies crosses between *C. tyzzeri* and *C.*
473 *parvum* revealed that crossovers are strongly suppressed and most chromosomes are inherited
474 uniparentally without crossovers [70]. Although we have not interrogated the nature of CENH3
475 binding sites in *C. tyzzeri*, differences in the recognition sequences or pattern of centromere
476 distribution (i.e. monocentric vs. holocentric) could result in suppression of hybrids due to miotic
477 or meiotic interference.
478

479 **Limitations and Future Studies**

480 Examination of the nuclear organization of *C. parvum* throughout the cell cycle revealed a
481 persistently diffuse centromere staining pattern, suggesting a holocentric chromosome structure.
482 During division, such multiple centromeric sites dispersed along the chromosome are expected to
483 bind centrosomes and thereby connect to microtubules for chromosome separation. Although we
484 visualized events consistent with this process in an artificial timeline, future studies using

485 fluorescent reporters could potentially provide more precise information on the formation of
486 centrosomes, coordinated assembly of microtubules, and nuclear division in *C. parvum*.
487 However, obtaining direct cytological data in support of holocentric centromeres and their
488 behavior during nuclear division will be challenging in this system because chromosomes do not
489 condense during division. Alternatively, it may be possible to explore the nature of centromeres
490 by examining the distribution of other conserved centrosomes and kinetochore binding proteins
491 during nuclear division. Such studies could shed further light on chromosome tethering in
492 nuclear division and provide invaluable insights into unique evolutionary adaptations in *C.*
493 *parvum*. Additionally, extending these studies to define how centromeres are organized in related
494 species could provide insight into mechanisms of diversification that drive speciation.
495

496 **Acknowledgements:**

497 We thank Jennifer Barks for assistance with cell culture, Dr. Wandy L. Beatty, Microbiology
498 Imaging Facility, Washington University School of Medicine in St. Louis, for assistance with
499 microscopy, and Dr. Kami Kim, Univ. South Florida, for providing the *T. gondii* CENH3-HA
500 line used here. We are grateful for helpful comments from Drs. Daniel E Goldberg, Douglas L.
501 Chalker, and Tim Schedl, Washington University and Dr. Lihua Xiao, South China Agricultural
502 University. Genome sequencing was performed by the GTAC Genome core at Washington
503 University in St Louis. Supported in part by the Graduate Research Fellowship Program,
504 National Science Foundation (to A.K.) and grant AI175150 from the National Institutes of
505 Health (to L.D.S.).
506

507 **Author contributions**

508 Conceptualization, AK, LDS; Data curation, AK, WH; Formal analysis, AK, WH; Funding
509 acquisition, LDS; Investigation, AK, WH, MK, LFJ; Methodology, AK, WH, MK, LFJ;
510 Resources, WK, WH, MK, LFJ; Validation, AK, WH; Visualization, AK, WH; Supervision,
511 LDS; Writing – original draft, AK, WH, LDS; Writing – review & editing, AK, WH, LDS.

512 **Data Sources and Availability:**

513 All materials described here are available from the corresponding author based on MTA.
514 Sequence for the CUT&RUN analyses have been deposited to the NCBI Bioproject #
515 PRJNA1330822.

516 **Declarations:**

517 The authors declare that they have no conflicts to disclose.

518

519 **MATERIALS & METHODS**

520 **Animal studies and ethical approval.**

521 Animal studies were approved by the Institutional Animal Studies Committee (School of
522 Medicine, Washington University in St. Louis). *Ifngr1*$^{-/-}$ mice (003288; Jackson Laboratories),
523 and NOD scid gamma mice (referred to as NSG) (005557; Jackson Laboratories) were bred in-
524 house in a specific-pathogen-free animal facility on a 12:12 light-dark cycle. Male and female
525 mice between 8 and 12 weeks of age were used for sex-matched groups used in crossing
526 experiments. Mice were co-housed with siblings of the same sex throughout the experiments.

527 **Cell culture.**

528 HCT-8 cells (Human ileocecal adenocarcinoma, ATCC CCL-244) derived from a human
529 ileocecal carcinoma were cultured in RPMI 1640 ATCC Modification medium supplemented
530 with 10% fetal bovine serum at 37 °C in a 5% CO_2 incubator. After trypsinization, 450,000 cells

531 were plated on glass coverslips in 24-well plates and used for experiments. Cells were confirmed
532 to be mycoplasma-free with the e-Myco plus Mycoplasma PCR detection kit.
533 **Immunofluorescence assays & microscopy.** Staining protocols have been previously described
534 and all antibodies are listed in **Table S2** [71]. Briefly, infected HCT-8 cultures were fixed with
535 4% formaldehyde 8-24 hpi, permeabilized with 0.1% Triton X-100, blocked with 1% bovine
536 serum albumin (BSA), stained with a primary antibody mixture for 1 h followed by secondary
537 antibodies for 1 h and Hoechst for 20 min. Primary antibodies were diluted for staining: anti-HA
538 (rat, 1:500), anti-Aldolase (ALD, rabbit, 1:1000) centrin-1 (mouse, 1:250), anti-Ty (mouse,
539 1:250), and anti-PH3 (rabbit, 1:500), NUP116 (rabbit, 1:100). All Alexa Fluor secondary
540 antibodies were diluted at 1:1000 and Hoechst was diluted 1:2000. Coverslips were mounted
541 onto microscope slides with Prolong Glass Antifade Mountant. Coverslips were visualized using
542 a Zeiss LSM880 laser scanning confocal microscope equipped with a 63x, 1.4 N.A. Zeiss Plan
543 Apochromat oil objective lens and Airy scan. Images were acquired with ZEN v2.1, v2.5
544 software and further analyzed using ImageJ. All staining experiments were performed
545 independently 2-3 times, and at least 2-5 fields of view were imaged per coverslip.
546 **Expansion Microscopy.** Ultrastructure expansion microscopy (U-ExM) was performed as
547 previously described [72]. HCT-8 cells were infected with the CENH3-3HA or CENH3-smHA
548 parasites and fixed following the same procedures used for standard immunofluorescence assays
549 or 16% methanol-free formaldehyde. Fixed samples were embedded overnight in a solution
550 containing 1% acrylamide and 0.7% formaldehyde to anchor proteins and prevent crosslinking.
551 The resulting gel was transferred into denaturation buffer and incubated at 95 °C. A second
552 expansion gel was polymerized on ice using a monomer mixture composed of 19% sodium
553 acrylate, 10% acrylamide, and 0.1% (1,2-Dihydroxyethylene) bisacrylamide, supplemented with

554 0.5% ammonium persulfate (APS) and 0.5% TEMED. Polymerized gels were denatured at 95 °C
555 for 90 min in denaturation buffer (200 mM SDS, 200 mM NaCl, 50 mM Tris-Base, pH 9.0) and
556 expanded overnight in ultrapure water. Expansion ratios were determined the following day by
557 measuring gel diameters. Gels were then shrunk in PBS and stained with primary antibodies
558 (rabbit anti-HA, rat anti-HA, or either rabbit anti-GFP antibodies at 1:200 and rat Pan-Cp,
559 1:500), followed by secondary antibodies (Alexa Fluor conjugates, 1:500) and Hoechst (1:500)
560 diluted in freshly prepared 2% PBS/BSA for 3, 12, or 24 h for primary antibodies and 2 h for
561 secondary antibodies at room temperature. After each staining step, gels were washed three times
562 in PBS/0.1% Tween for 10 min. Stained gels were re-expanded overnight in ultrapure water
563 before imaging. Images were acquired using a Zeiss LSM880 laser scanning confocal
564 microscope equipped with a 63x, 1.4 N.A. Zeiss Plan-Apochromat oil objective and ZEN v2.1 or
565 v2.5 software.
566 **Immuno-electron Microscopy.** Immuno-electron microscopy (EM) was performed as
567 previously described using CENH3-3HA and CENH3-smHA parasites [73]. HCT-8 monolayers
568 were grown in 6-well plates and reached confluence before infection with transgenic *C. parvum*
569 oocysts. After a 20-h incubation, cultures were washed twice in DPBS and fixed for 1 h at 4 °C
570 in freshly prepared fixative consisting of 4% paraformaldehyde and 0.05% glutaraldehyde in
571 100 mM PIPES supplemented with 0.5 mM $MgCl_2$ (pH 7.2). Fixed samples were embedded in
572 10% gelatin and subsequently infiltrated overnight at 4 °C with a cryoprotectant solution of
573 2.3 M sucrose and 20% polyvinyl pyrrolidone prepared in PIPES/$MgCl_2$. Blocks were trimmed,
574 rapidly frozen in liquid nitrogen, and sectioned using a Leica Ultracut UCT7
575 cryo-ultramicrotome. Ultrathin sections (50 nm) were blocked for 30 min in a mixture of 5%
576 fetal bovine serum and 5% normal goat serum, followed by incubation with rabbit anti-HA, rat

577 anti-HA, or either of the rabbit anti-GFP antibodies (1:1000) for 1 h at room temperature. After
578 rinsing in blocking buffer, sections were labeled for 1 h with 18 nm colloidal gold–conjugated
579 goat anti-rabbit IgG (H+L) diluted 1:20. Labeled sections were then contrasted with 0.3% uranyl
580 acetate in 2% methyl cellulose and imaged using a JEOL 1200 EX transmission electron
581 microscope equipped with an AMT 8-megapixel digital camera and AMT Image Capture Engine
582 v6.0.2. Control sections processed in parallel without primary antibody were included in all
583 experiments.

584 **CRISPR/Cas9 plasmid construction.**

585 ***Plasmid construction***

586 Primers used to generate the following plasmids were ordered from IDT and all sequences are
587 found in **Table S3**. SnapGene (v7.1.1) and NEBuilder Assembly Tool (v2.9.0) were used to
588 construct plasmid maps and design primers.

589 The CENH3-3HA tagging plasmid was generated using the previously described ABC-3HA
590 tagging plasmid [73] by replacing the C-terminal and 3'UTR sequences with equivalent regions
591 from the *Cp*CENH3 gene amplified from *C. parvum* cDNA to generate the tagging plasmid
592 CENH3-3HA-Nluc-P2A-Neo^{R}.

593 The 3HA-CENH3- GBP-3Ty tagging plasmid was created via a seven-way Gibson assembly
594 combining a backbone generated from the TK-GFP-Nluc-P2A-Neo^{R}-TK homology tagging
595 plasmid previously generated in our lab [74] together with the following fragments: 1) The 5'
596 homology region of CENH3 (500 bp), the CENH3 CDS, a portion of the 3' homology region of
597 CENH3 (216 bp) were amplified from the CENH3-3HA tagging plasmid described above. 2)
598 The 3HA-pLinker region was amplified from a TK-3HA-CENH3-Nluc-P2A-Neo^{R}-TK plasmid
599 (data not shown in this study), 3) the GBP CDS was amplified from *C. parvum* genomic DNA,

600 4) the pLinker-3Ty sequence was amplified from a tagging plasmid previously generated in our
601 lab [73], and 5) the P2A skip peptide sequence was generated as a gBlock Gene Fragment from
602 Azenta. The U6:sgTK plasmid previously generated in our lab was utilized for all experiments
603 with TK locus replacement repair plasmids [74].

604 The H3.1-3HA and H3.2-3HA tagging plasmids were generated via Gibson assembly using
605 the 3HA-CENH3-GBP-3Ty plasmid to provide a backbone, the pLinker-3HA region was
606 amplified from the CENH3-3HA tagging plasmid described above, and the CDS regions for
607 H3.1 and H3.2 were amplified from *C. parvum* genomic DNA.

608 The GBP-3HA tagging plasmid was generated using the CENH3-3HA tagging plasmid
609 described above for the backbone and replacing the C-terminal and 3'UTR sequences with the
610 GBP CDS sequence amplified from *C. parvum* genomic DNA.

611 CENH3 and GBP CRISPR/Cas9 plasmids were created via Gibson assembly of the
612 linearized backbone amplified from the TK CRISPR/Cas9 plasmid (Addgene 122852) and an
613 oligonucleotide with the sgRNA specific for the CENH3 or GBP gene [74]. The Eukaryotic
614 Pathogen CRISPR guide RNA/DNA Design tool (http://grna.ctegd.uga.edu) was used to identify
615 CENH3 and GBP sgRNA sequences.

616 **Amplifying transgenic parasites in mice.**

617 The transfection and amplification of parasites in immunocompromised mice were conducted as
618 previously described [74-77]. Briefly, $1x10^8$ freshly excysted sporozoites were electroporated
619 with 100 µg of repair plasmid and 66 µg of CRISPR/Cas9 plasmid, then resuspended in 300 µL
620 of cold DPBS. *Ifngr1*$^{-/-}$ mice were first orally gavaged with an 8% (wt/vol) sodium bicarbonate
621 solution to neutralize stomach acid, followed by the administration of the electroporated
622 sporozoites. To facilitate the selection of transgenic parasites, paromomycin (16 g/L) was

623 provided in the drinking water 24 h post-infection. Fecal pellets were collected at intervals post-
624 infection for luciferase assays and diagnostic PCR analysis to verify parasite growth and proper
625 gene insertion. Oocysts were isolated from fecal material using bleach treatment, and 20,000
626 oocysts per mouse were employed for a subsequent round of amplification in NSG mice.
627 **Luciferase assays for mouse experiments.** Fecal samples collected from infected mice were
628 analyzed with the Promega Nano-Glo luciferase assay kit, as previously described [77]. The
629 luciferase activity was measured using the BioTek Cytation 3 cell imaging multi-mode reader.
630 The number of relative luminescence units per milligram of feces was obtained by dividing the
631 average values from two technical replicates by the fecal sample weight.
632 **Quantifying oocyst shedding in mouse experiments.** DNA was extracted from fecal pellets
633 collected from infected mice using the QIAamp PowerFecal DNA kit, following previously
634 established methods [74, 76, 77]. Quantitative PCR (qPCR) analysis was conducted to determine
635 the number of oocysts at each time point based on *C. parvum* glyceraldehyde-3-phosphate
636 dehydrogenase (GAPDH) primers and a standard curve derived from a dilution series (**S2 Table**)
637 [74]. Genomic DNA (gDNA) amounts were quantified using the QuantStudio 3 real-time PCR
638 system.
639 **Confirmation of insertions in transgenic parasites by PCR.**
640 To confirm the correct integration of the homology repair template, extracted gDNA from
641 murine fecal samples and wild type controls were used as the template. PCR amplification was
642 performed using 1 μL of the extracted gDNA, Q5 Hot Start high-fidelity 2X master mix or
643 PrimeSTAR GXL premix (TaKaRa), and primers at a final concentration of 500 nM on a Veriti
644 96-well thermal cycler. All PCR products were resolved on a 1% agarose gel containing GelRed
645 (1:10,000) and visualized using the ChemiDoc MP imaging system.

646 **Oocyst purification from fecal material and storage.**

647 The *C. parvum* isolate AUCP -1 used for transfections was purified from fecal material collected
648 from male Holstein calves at the University of Illinois at Urbana-Champaign [78]. All
649 procedures involving the calves received approval from the Institutional Animal Care and Use
650 Committee (IACUC). Transgenic oocysts were purified in-house from fecal material collected
651 from NSG mice, using a saturated sodium chloride solution for oocyst flotation [79]. Post-
652 purification, oocysts were stored at 4°C in phosphate-buffered saline (PBS) for up to three
653 months following fecal collection.

654 **Structural predictions**

655 The protein structure of the G-quadruplex binding protein (GBP, *cgd1*_3530) was predicted
656 using Alphafold 3 (www.alphafoldserver.com). Using ChimeraX
657 (https://www.cgl.ucsf.edu/chimerax/), we modeled how the G-quadruplex structure formed by
658 the *Cp*GBP repetitive binding sequence (GGTTA) [51] interacts and is stabilized by the CpGBP
659 protein.

660 **Channel colocalization quantification**

661 Co-localization analysis was performed using the Coloc2 plugin (FIJI/ImageJ), using default
662 thresholding parameters. A 2D intensity histogram was generated as part of the Coloc2 output to
663 visualize the pixel-wise distribution of intensities from both channels and a Pearson correlation
664 coefficient was quantified.

665 **Parasite Preparation and Lysis for CUT&RUN experiments.**

666 The CENH3-3HA line of *T. gondii* [27] was obtained from the laboratory of Dr. Kami Kim at
667 University of South Florida. *Tg*CENH3-3HA tachyzoites were propagated in human foreskin
668 fibroblasts and harvested using established protocols [80]. *C. parvum* sporozoites ($4x10^7$) and *T.*

669 *gondii* tachyzoites ($1x10^7$) were centrifuged at 2,500 RPM for 5 min, supernatants removed, and
670 parasites were resuspended in 2 mL of cold parasite lysis buffer (10 mM HEPES pH 7.9, 1.5 mM
671 MgCl2, 10 mM KCl, 0.65% NP40 (supplemented with IGEPAL) and 0.5 mM PMSF
672 (supplemented with cOmplete EDTA free protease inhibitor cocktail and sterile distilled H_2O),
673 incubated for 10 min on ice, and centrifuged at 3,000 RPM for 10 min at 4°C (previously
674 described in [81, 82]).

675 **CUT&RUN Processing, Library Preparation, Quality Control & Sequencing.**

676 Following lysis treatment, the lysis buffer was removed, and the nuclei pellet was washed
677 following the CUT&RUN Kit Version 4 protocol (EpiCypher, Inc, Catalog No. 14-1048).
678 Isolated nuclei were incubated with either 1.0 µg of rat anti-HA antibody, 0.5 µg of rabbit anti-
679 H3K4me3 positive control antibody, or 0.5 µg of mouse anti-IgG negative control antibody.
680 Chromatin digestion and release steps were performed according to the EpiCypher protocol, and
681 5 ng of CUT&RUN enriched DNA was used for library preparation according to the CUT&RUN
682 Library Prep Kit User Manual Version 1.5 (EpiCypher, Inc, Catalog No. 14-1001). The
683 concentrations of CUT&RUN library samples were determined via Qubit and quality control
684 were assessed with an Agilent 4200 TapeStation.

685 **CUT&RUN Analysis & Visualization.**

686 Multiple CUT&RUN runs were preformed to obtain biological replicates of each sample. DNA
687 products were sequenced on an Illumina NovaSeq 6000 using 150-bp paired-ends at the GTAC
688 sequencing core at Washington University in St. Louis. Sequence reads obtained from Illumina
689 were trimmed for adapter sequences and poor sequence quality (phred score < 25 and trimmed
690 length < 50) using fastp v0.23.4. The trimmed reads were mapped to the reference *C. parvum*
691 IOWA-CDC genome using BWA-MEM v0.7.17 [83]. Duplicate reads were marked and

removed in the bam files using the MarkDuplicates algorithm of picard v3.1.1 (https://broadinstitute.github.io/picard/) with REMOVE_DUPLICATES=true, CREATE_INDEX=true, and ASSUME_SORTED=true. Reads with mapping lengths less than 50 bp were further removed from the bam files using SAMtools v1.7 (http://samtools.sourceforge.net/). Genome coverage and sequence depth were estimated using the mpileup algorithm of SAMtools. The read depth of each locus was normalized by dividing by the total number of counts for all loci, then scaled by multiplying by the number of loci in the genome. Input counts were subtracted from negative control counts. Data was visualized by a R package 'ggplot2' (https://www.rdocumentation.org/packages/ggplot2). Motifs within centromeric windows were identified using MEME v5.5.8 (https://meme-suite.org/meme/tools/meme). Chromosomal distributions of intergenic regions, centromeric windows, and motifs were visualized with Circos plot generated in TBtools-II v2.311 (https://github.com/CJ-Chen/TBtools-II).

706 **REFERENCES:**
707

708 1. Tyzzer E. An extracellular coccidium, Cryptosporidium muris (gen. et sp. nov.), of the
709 gastric glands of the common mouse. J Med Res. 1910;23:487-509. PubMed Central
710 PMCID: PMCPMC2098948.
711 2. Greenberg PD, Koch J, Cello JP. Diagnosis of Cryptosporidium parvum in patients with
712 severe diarrhea and AIDS. Dig Dis Sci. 1996;41(11):2286-90.
713 3. Striepen B. Parasitic infections: Time to tackle cryptosporidiosis. Nature.
714 2013;503(7475):189-91. PubMed Central PMCID: PMC24236315.
715 4. Tzipori S, Widmer G. A hundred-year retrospective on cryptosporidiosis. Trends Parasitol.
716 2008;24(4):184-9. Epub 20080307. doi: 10.1016/j.pt.2008.01.002. PubMed PMID:
717 18329342; PubMed Central PMCID: PMCPMC2716703.
718 5. Sow SO, Muhsen K, Nasrin D, Blackwelder WC, Wu Y, Farag TH, et al. The Burden of
719 Cryptosporidium Diarrheal Disease among Children < 24 Months of Age in
720 Moderate/High Mortality Regions of Sub-Saharan Africa and South Asia, Utilizing Data
721 from the Global Enteric Multicenter Study (GEMS). PLoS Negl Trop Dis.
722 2016;10(5):e0004729. Epub 2016/05/25. doi: 10.1371/journal.pntd.0004729. PubMed
723 PMID: 27219054; PubMed Central PMCID: PMCPMC4878811.
724 6. Kotloff KL, Nataro JP, Blackwelder WC, Nasrin D, Farag TH, Panchalingam S, et al. Burden
725 and aetiology of diarrhoeal disease in infants and young children in developing countries
726 (the Global Enteric Multicenter Study, GEMS): a prospective, case-control study. Lancet.
727 2013;382(9888):209-22.
728 7. Wanyiri JW, Kanyi H, Maina S, Wang DE, Steen A, Ngugi P, et al. Cryptosporidiosis in
729 HIV/AIDS patients in Kenya: clinical features, epidemiology, molecular characterization
730 and antibody responses. Am J Trop Med Hyg. 2014;91(2):319-28. Epub 2014/05/29. doi:
731 10.4269/ajtmh.13-0254. PubMed PMID: 24865675; PubMed Central PMCID:
732 PMCPMC4125256.
733 8. Funkhouser-Jones LJ, Ravindran S, Sibley LD. Defining Stage-Specific Activity of Potent
734 New Inhibitors of Cryptosporidium parvum Growth In Vitro. mBio. 2020;11(2). Epub
735 2020/03/05. doi: 10.1128/mBio.00052-20. PubMed PMID: 32127445; PubMed Central
736 PMCID: PMCPMC7064746.
737 9. English ED, Guerin A, Tandel J, Striepen B. Live imaging of the Cryptosporidium parvum
738 life cycle reveals direct development of male and female gametes from type I meronts.
739 PLoS Biol. 2022;20(4):e3001604. Epub 2022/04/19. doi: 10.1371/journal.pbio.3001604.
740 PubMed PMID: 35436284; PubMed Central PMCID: PMCPMC9015140.
741 10. Beyer TV, Svezhova NV, Sidorenko NV, Khokhlov SE. Cryptosporidium parvum (Coccidia,
742 Apicomplexa): Some new ultrastructural observations on its endogenous development.
743 European Journal of Protistology. 2000;36(2):151-9. doi: 10.1016/s0932-4739(00)80034-
744 6.
745 11. Pohlenz J, Bemrick WJ, Moon HW, Cheville NF. Bovine cryptosporidiosis: a transmission
746 and scanning electron microscopic study of some stages in the life cycle and of the host-
747 parasite relationship. Vet Pathol. 1978;15(3):417-27. Epub 1978/05/01. doi:
748 10.1177/030098587801500318. PubMed PMID: 98896.
749 12. Tzipori S, McCartney E, Lawson GH, Rowland AC, Campbell I. Experimental infection of
750 piglets with cryptosporidium. Res Vet Sci. 1981;31(3):358-68. Epub 1981/11/01. PubMed
751 PMID: 7342229.

752 13. Current WL, Reese NC. A comparison of endogenous development of three isolates of
753 Cryptosporidium in suckling mice. J Protozool. 1986;33(1):98-108. Epub 1986/02/01.
754 PubMed PMID: 3959014.
755 14. Keithly JS, Langreth SG, Buttle KF, Mannella CA. Electron tomographic and ultrastructural
756 analysis of the Cryptosporidium parvum relict mitochondrion, its associated membranes,
757 and organelles. J Eukaryot Microbiol. 2005;52(2):132-40. Epub 2005/04/09. doi:
758 10.1111/j.1550-7408.2005.04-3317.x. PubMed PMID: 15817118.
759 15. Wilke G. Development of an in vitro Culture System for Cryptosporidium parvum. Theses
760 and Dissertations: Washington University in St. Louis; 2020.
761 16. White MW, Suvorova ES. Apicomplexa Cell Cycles: Something Old, Borrowed, Lost, and
762 New. Trends Parasitol. 2018;34(9):759-71. Epub 20180802. doi:
763 10.1016/j.pt.2018.07.006. PubMed PMID: 30078701; PubMed Central PMCID:
764 PMCPMC6157590.
765 17. Striepen B, Jordan CN, Reiff S, van Dooren GG. Building the perfect parasite: cell division
766 in apicomplexa. PLoS Pathog. 2007;3(6):e78. doi: 10.1371/journal.ppat.0030078. PubMed
767 PMID: 17604449; PubMed Central PMCID: PMCPMC1904476.
768 18. Gissot M, Walker R, Delhaye S, Huot L, Hot D, Tomavo S. Toxoplasma gondii
769 chromodomain protein 1 binds to heterochromatin and colocalises with centromeres and
770 telomeres at the nuclear periphery. PLoS One. 2012;7(3):e32671. Epub 20120309. doi:
771 10.1371/journal.pone.0032671. PubMed PMID: 22427862; PubMed Central PMCID:
772 PMCPMC3302879.
773 19. Duraisingh MT, Voss TS, Marty AJ, Duffy MF, Good RT, Thompson JK, et al.
774 Heterochromatin silencing and locus repositioning linked to regulation of virulence genes
775 in Plasmodium falciparum. Cell. 2005;121(1):13-24. doi: 10.1016/j.cell.2005.01.036.
776 PubMed PMID: 15820675.
777 20. del Cacho E, Pages M, Gallego M, Barbero JL, Monteagudo L, Sanchez-Acedo C. Meiotic
778 chromosome pairing and bouquet formation during Eimeria tenella sporulation. Int J
779 Parasitol. 2010;40(4):453-62. Epub 20091029. doi: 10.1016/j.ijpara.2009.09.008. PubMed
780 PMID: 19837073.
781 21. Dey G, Culley S, Curran S, Schmidt U, Henriques R, Kukulski W, et al. Closed mitosis
782 requires local disassembly of the nuclear envelope. Nature. 2020;585(7823):119-23. Epub
783 20200826. doi: 10.1038/s41586-020-2648-3. PubMed PMID: 32848252; PubMed Central
784 PMCID: PMCPMC7610560.
785 22. Matthews H, Duffy CW, Merrick CJ. Checks and balances? DNA replication and the cell
786 cycle in Plasmodium. Parasit Vectors. 2018;11(1):216. Epub 20180327. doi:
787 10.1186/s13071-018-2800-1. PubMed PMID: 29587837; PubMed Central PMCID:
788 PMCPMC5872521.
789 23. Rout MP, Obado SO, Schenkman S, Field MC. Specialising the parasite nucleus: Pores,
790 lamins, chromatin, and diversity. PLoS Pathog. 2017;13(3):e1006170. Epub 20170302.
791 doi: 10.1371/journal.ppat.1006170. PubMed PMID: 28253370; PubMed Central PMCID:
792 PMCPMC5333908.
793 24. Suvorova ES, Francia M, Striepen B, White MW. A novel bipartite centrosome coordinates
794 the apicomplexan cell cycle. PLoS Biol. 2015;13(3):e1002093. Epub 20150303. doi:
795 10.1371/journal.pbio.1002093. PubMed PMID: 25734885; PubMed Central PMCID:
796 PMCPMC4348508.

797 25. Chen CT, Kelly M, Leon J, Nwagbara B, Ebbert P, Ferguson DJ, et al. Compartmentalized
798 Toxoplasma EB1 bundles spindle microtubules to secure accurate chromosome
799 segregation. Mol Biol Cell. 2015;26(25):4562-76. Epub 20151014. doi: 10.1091/mbc.E15-
800 06-0437. PubMed PMID: 26466679; PubMed Central PMCID: PMCPMC4678015.
801 26. Hoeijmakers WA, Flueck C, Francoijs KJ, Smits AH, Wetzel J, Volz JC, et al. Plasmodium
802 falciparum centromeres display a unique epigenetic makeup and cluster prior to and
803 during schizogony. Cell Microbiol. 2012;14(9):1391-401. Epub 20120515. doi:
804 10.1111/j.1462-5822.2012.01803.x. PubMed PMID: 22507744.
805 27. Brooks CF, Francia ME, Gissot M, Croken MM, Kim K, Striepen B. Toxoplasma gondii
806 sequesters centromeres to a specific nuclear region throughout the cell cycle. Proc Natl
807 Acad Sci U S A. 2011;108(9):3767-72. Epub 20110214. doi: 10.1073/pnas.1006741108.
808 PubMed PMID: 21321216; PubMed Central PMCID: PMCPMC3048097.
809 28. Arnot DE, Ronander E, Bengtsson DC. The progression of the intra-erythrocytic cell cycle of
810 Plasmodium falciparum and the role of the centriolar plaques in asynchronous mitotic
811 division during schizogony. Int J Parasitol. 2011;41(1):71-80. Epub 20100917. doi:
812 10.1016/j.ijpara.2010.07.012. PubMed PMID: 20816844.
813 29. Iwanaga S, Khan SM, Kaneko I, Christodoulou Z, Newbold C, Yuda M, et al. Functional
814 identification of the Plasmodium centromere and generation of a Plasmodium artificial
815 chromosome. Cell Host Microbe. 2010;7(3):245-55. doi: 10.1016/j.chom.2010.02.010.
816 PubMed PMID: 20227667; PubMed Central PMCID: PMCPMC2996609.
817 30. Absalon S. A dynamic barrier: remodeling of the nuclear envelope during closed mitosis in
818 malaria parasites. mSphere. 2025;10(7):e0099924. Epub 20250609. doi:
819 10.1128/msphere.00999-24. PubMed PMID: 40488521; PubMed Central PMCID:
820 PMCPMC12306155.
821 31. Weiner A, Dahan-Pasternak N, Shimoni E, Shinder V, von Huth P, Elbaum M, et al. 3D
822 nuclear architecture reveals coupled cell cycle dynamics of chromatin and nuclear pores in
823 the malaria parasite Plasmodium falciparum. Cell Microbiol. 2011;13(7):967-77. Epub
824 20110428. doi: 10.1111/j.1462-5822.2011.01592.x. PubMed PMID: 21501361.
825 32. Kursel LE, Malik HS. Centromeres. Curr Biol. 2016;26(12):R487-R90. doi:
826 10.1016/j.cub.2016.05.031. PubMed PMID: 27326706.
827 33. Hegemann JH, Fleig UN. The centromere of budding yeast. Bioessays. 1993;15(7):451-60.
828 doi: 10.1002/bies.950150704. PubMed PMID: 8379948.
829 34. Kelly JM, McRobert L, Baker DA. Evidence on the chromosomal location of centromeric
830 DNA in Plasmodium falciparum from etoposide-mediated topoisomerase-II cleavage.
831 Proc Natl Acad Sci U S A. 2006;103(17):6706-11. Epub 20060414. doi:
832 10.1073/pnas.0510363103. PubMed PMID: 16617116; PubMed Central PMCID:
833 PMCPMC1458945.
834 35. Viera A, Page J, Rufas JS. Inverted meiosis: the true bugs as a model to study. Genome Dyn.
835 2009;5:137-56. doi: 10.1159/000166639. PubMed PMID: 18948713.
836 36. Mandrioli M, Manicardi GC. Holocentric chromosomes. PLoS Genet. 2020;16(7):e1008918.
837 Epub 20200730. doi: 10.1371/journal.pgen.1008918. PubMed PMID: 32730246; PubMed
838 Central PMCID: PMCPMC7392213.
839 37. Marques A, Drinnenberg IA. Same but different: Centromere regulations in holocentric
840 insects and plants. Curr Opin Cell Biol. 2025;93:102484. Epub 20250220. doi:
841 10.1016/j.ceb.2025.102484. PubMed PMID: 39983583.

842 38. Bensasson D. Evidence for a high mutation rate at rapidly evolving yeast centromeres. BMC
843 Evol Biol. 2011;11:211. Epub 20110718. doi: 10.1186/1471-2148-11-211. PubMed
844 PMID: 21767380; PubMed Central PMCID: PMCPMC3155921.
845 39. Csink AK, Henikoff S. Something from nothing: the evolution and utility of satellite repeats.
846 Trends Genet. 1998;14(5):200-4. doi: 10.1016/s0168-9525(98)01444-9. PubMed PMID:
847 9613205.
848 40. Talbert PB, Henikoff S. Centromeres drive and take a break. Chromosome Res.
849 2025;33(1):17. Epub 20250804. doi: 10.1007/s10577-025-09777-z. PubMed PMID:
850 40759764; PubMed Central PMCID: PMCPMC12321929.
851 41. Henikoff S, Ahmad K, Malik HS. The centromere paradox: stable inheritance with rapidly
852 evolving DNA. Science. 2001;293(5532):1098-102. doi: 10.1126/science.1062939.
853 PubMed PMID: 11498581.
854 42. Talbert PB, Henikoff S. What makes a centromere? Exp Cell Res. 2020;389(2):111895. Epub
855 20200206. doi: 10.1016/j.yexcr.2020.111895. PubMed PMID: 32035948.
856 43. Skene PJ, Henikoff S. An efficient targeted nuclease strategy for high-resolution mapping of
857 DNA binding sites. Elife. 2017;6. Epub 20170116. doi: 10.7554/eLife.21856. PubMed
858 PMID: 28079019; PubMed Central PMCID: PMCPMC5310842.
859 44. Herrera-Solorio AM, Vembar SS, MacPherson CR, Lozano-Amado D, Meza GR,
860 Xoconostle-Cazares B, et al. Clipped histone H3 is integrated into nucleosomes of DNA
861 replication genes in the human malaria parasite Plasmodium falciparum. EMBO Rep.
862 2019;20(4). Epub 20190304. doi: 10.15252/embr.201846331. PubMed PMID: 30833341;
863 PubMed Central PMCID: PMCPMC6446197.
864 45. Verma G, Surolia N. Plasmodium falciparum CENH3 is able to functionally complement
865 Cse4p and its, C-terminus is essential for centromere function. Mol Biochem Parasitol.
866 2013;192(1-2):21-9. Epub 20131206. doi: 10.1016/j.molbiopara.2013.11.002. PubMed
867 PMID: 24316361.
868 46. Naumov A, Kratzer S, Ting LM, Kim K, Suvorova ES, White MW. The Toxoplasma
869 Centrocone Houses Cell Cycle Regulatory Factors. mBio. 2017;8(4). Epub 20170822. doi:
870 10.1128/mBio.00579-17. PubMed PMID: 28830940; PubMed Central PMCID:
871 PMCPMC5565962.
872 47. Mahajan B, Selvapandiyan A, Gerald NJ, Majam V, Zheng H, Wickramarachchi T, et al.
873 Centrins, cell cycle regulation proteins in human malaria parasite Plasmodium falciparum.
874 J Biol Chem. 2008;283(46):31871-83. Epub 20080808. doi: 10.1074/jbc.M800028200.
875 PubMed PMID: 18693242.
876 48. Ay F, Bunnik EM, Varoquaux N, Bol SM, Prudhomme J, Vert JP, et al. Three-dimensional
877 modeling of the P. falciparum genome during the erythrocytic cycle reveals a strong
878 connection between genome architecture and gene expression. Genome Res.
879 2014;24(6):974-88. Epub 20140326. doi: 10.1101/gr.169417.113. PubMed PMID:
880 24671853; PubMed Central PMCID: PMCPMC4032861.
881 49. Bunnik EM, Cook KB, Varoquaux N, Batugedara G, Prudhomme J, Cort A, et al. Changes in
882 genome organization of parasite-specific gene families during the Plasmodium
883 transmission stages. Nat Commun. 2018;9(1):1910. Epub 20180515. doi: 10.1038/s41467-
884 018-04295-5. PubMed PMID: 29765020; PubMed Central PMCID: PMCPMC5954139.
885 50. Hollin T, Le Roch KG. From Genes to Transcripts, a Tightly Regulated Journey in
886 Plasmodium. Front Cell Infect Microbiol. 2020;10:618454. Epub 20201217. doi:

887 10.3389/fcimb.2020.618454. PubMed PMID: 33425787; PubMed Central PMCID:
888 PMCPMC7793691.
889 51. Liu C, Wang L, Lancto CA, Abrahamsen MS. Characterization of a Cryptosporidium parvum
890 protein that binds single-stranded G-strand telomeric DNA. Mol Biochem Parasitol.
891 2009;165(2):132-41. Epub 20090204. doi: 10.1016/j.molbiopara.2009.01.013. PubMed
892 PMID: 19428660.
893 52. McIntosh JR. Mitosis. Cold Spring Harb Perspect Biol. 2016;8(9). Epub 20160901. doi:
894 10.1101/cshperspect.a023218. PubMed PMID: 27587616; PubMed Central PMCID:
895 PMCPMC5008068.
896 53. Perez-Cadahia B, Drobic B, Davie JR. H3 phosphorylation: dual role in mitosis and
897 interphase. Biochem Cell Biol. 2009;87(5):695-709. doi: 10.1139/O09-053. PubMed
898 PMID: 19898522.
899 54. Guizetti J, Martins RM, Guadagnini S, Claes A, Scherf A. Nuclear pores and perinuclear
900 expression sites of var and ribosomal DNA genes correspond to physically distinct regions
901 in Plasmodium falciparum. Eukaryot Cell. 2013;12(5):697-702. Epub 20130308. doi:
902 10.1128/EC.00023-13. PubMed PMID: 23475702; PubMed Central PMCID:
903 PMCPMC3647773.
904 55. Gerald N, Mahajan B, Kumar S. Mitosis in the human malaria parasite Plasmodium
905 falciparum. Eukaryot Cell. 2011;10(4):474-82. Epub 20110211. doi: 10.1128/EC.00314-
906 10. PubMed PMID: 21317311; PubMed Central PMCID: PMCPMC3127633.
907 56. Francia ME, Striepen B. Cell division in apicomplexan parasites. Nat Rev Microbiol.
908 2014;12(2):125-36. Epub 20140102. doi: 10.1038/nrmicro3184. PubMed PMID:
909 24384598.
910 57. Steiner FA, Henikoff S. Holocentromeres are dispersed point centromeres localized at
911 transcription factor hotspots. Elife. 2014;3:e02025. Epub 20140101. doi:
912 10.7554/eLife.02025. PubMed PMID: 24714495; PubMed Central PMCID:
913 PMCPMC3975580.
914 58. Xia J, Venkat A, Bainbridge RE, Reese ML, Le Roch KG, Ay F, et al. Third-generation
915 sequencing revises the molecular karyotype for Toxoplasma gondii and identifies
916 emerging copy number variants in sexual recombinants. Genome Res. 2021;31(5):834-51.
917 Epub 20210427. doi: 10.1101/gr.262816.120. PubMed PMID: 33906962; PubMed Central
918 PMCID: PMCPMC8092015.
919 59. Blauwkamp J, Ambekar SV, Hussain T, Mair GR, Beck JR, Absalon S. Nuclear pore
920 complexes undergo Nup221 exchange during blood-stage asexual replication of parasites.
921 Msphere. 2024;9(12). doi: 10.1128/msphere.00750-24. PubMed PMID:
922 WOS:001352594000001.
923 60. Haase R, Puthenpurackal A, Maco B, Guerin A, Soldati-Favre D. gamma-tubulin complex
924 controls the nucleation of tubulin-based structures in Apicomplexa. Mol Biol Cell.
925 2024;35(9):ar121. Epub 20240724. doi: 10.1091/mbc.E24-03-0100. PubMed PMID:
926 39046777; PubMed Central PMCID: PMCPMC11449391.
927 61. Edwards-Smallbone J, Jensen AL, Roberts LE, Totanes FIG, Hart SR, Merrick CJ.
928 Plasmodium falciparum GBP2 Is a Telomere-Associated Protein That Binds to G-
929 Quadruplex DNA and RNA. Front Cell Infect Microbiol. 2022;12:782537. Epub
930 20220222. doi: 10.3389/fcimb.2022.782537. PubMed PMID: 35273922; PubMed Central
931 PMCID: PMCPMC8902816.

932 62. Zhao N, Gong P, Li Z, Cheng B, Li J, Yang Z, et al. Identification of a telomeric DNA-
933 binding protein in Eimeria tenella. Biochem Biophys Res Commun. 2014;451(4):599-602.
934 Epub 20140813. doi: 10.1016/j.bbrc.2014.08.030. PubMed PMID: 25128826.
935 63. Melters DP, Paliulis LV, Korf IF, Chan SW. Holocentric chromosomes: convergent
936 evolution, meiotic adaptations, and genomic analysis. Chromosome Res. 2012;20(5):579-
937 93. doi: 10.1007/s10577-012-9292-1. PubMed PMID: 22766638.
938 64. Lucek K, Augustijnen H, Escudero M. A holocentric twist to chromosomal speciation?
939 Trends Ecol Evol. 2022;37(8):655-62. Epub 20220426. doi: 10.1016/j.tree.2022.04.002.
940 PubMed PMID: 35484024.
941 65. Helsen J, Ramachandran K, Sherlock G, Dey G. Progressive coevolution of the yeast
942 centromere and kinetochore. Nature. 2025. Epub 20251126. doi: 10.1038/s41586-025-
943 09779-1. PubMed PMID: 41299172; PubMed Central PMCID: PMCPMC12925627.
944 66. Funkhouser-Jones LJ, Xu R, Wilke G, Fu Y, Schriefer LA, Makimaa H, et al. Microbiota-
945 produced indole metabolites disrupt mitochondrial function and inhibit Cryptosporidium
946 parvum growth. Cell Rep. 2023;42(7):112680. Epub 2023/06/29. doi:
947 10.1016/j.celrep.2023.112680. PubMed PMID: 37384526.
948 67. Pardy RD, Wallbank BA, Striepen B, Hunter CA. Immunity to Cryptosporidium: insights
949 into principles of enteric responses to infection. Nat Rev Immunol. 2024;24(2):142-55.
950 Epub 20230911. doi: 10.1038/s41577-023-00932-3. PubMed PMID: 37697084.
951 68. Martinez-Perez E, Schvarzstein M, Barroso C, Lightfoot J, Dernburg AF, Villeneuve AM.
952 Crossovers trigger a remodeling of meiotic chromosome axis composition that is linked to
953 two-step loss of sister chromatid cohesion. Genes Dev. 2008;22(20):2886-901. doi:
954 10.1101/gad.1694108. PubMed PMID: 18923085; PubMed Central PMCID:
955 PMCPMC2569886.
956 69. Kimball A, Funkhouser-Jones L, Huang W, Xu R, Witola WH, Sibley LD. Mendelian
957 segregation and high recombination rates facilitate genetic analyses in Cryptosporidium
958 parvum. PLoS Genet. 2024;20(6):e1011162. Epub 20240617. doi:
959 10.1371/journal.pgen.1011162. PubMed PMID: 38885280; PubMed Central PMCID:
960 PMCPMC11213348.
961 70. Shaw S, Cohn IS, Baptista RP, Xia G, Melillo B, Agyabeng-Dadzie F, et al. Genetic crosses
962 within and between species of Cryptosporidium. Proc Natl Acad Sci U S A.
963 2024;121(1):e2313210120. Epub 2023/12/26. doi: 10.1073/pnas.2313210120. PubMed
964 PMID: 38147547; PubMed Central PMCID: PMCPMC10769859.
965 71. Wilke G, Ravindran S, Funkhouser-Jones L, Barks J, Wang Q, VanDussen KL, et al.
966 Monoclonal antibodies to intracellular stages of *Cryptosporidium parvum* define life cycle
967 progression in vitro. Msphere. 2018;3(3):e00124-18. Epub 2018/06/01. doi:
968 10.1128/mSphere.00124-18. PubMed PMID: 29848759; PubMed Central PMCID:
969 PMCPMC5976880.
970 72. Dos Santos Pacheco N, Soldati-Favre D. Coupling Auxin-Inducible Degron System with
971 Ultrastructure Expansion Microscopy to Accelerate the Discovery of Gene Function in
972 Toxoplasma gondii. Methods Mol Biol. 2021;2369:121-37. doi: 10.1007/978-1-0716-
973 1681-9_8. PubMed PMID: 34313987.
974 73. Xu R, Beatty WL, Greigert V, Witola WH, Sibley LD. Multiple pathways for glucose
975 phosphate transport and utilization support growth of Cryptosporidium parvum. Nat
976 Commun. 2024;15(1):380. Epub 20240109. doi: 10.1038/s41467-024-44696-3. PubMed
977 PMID: 38191884; PubMed Central PMCID: PMCPMC10774378.

978 74. Wilke G, Funkhouser-Jones L, Wang Y, Ravindran S, Wang Q, Beatty WL, et al. Forward
979 genetics in *Cryptosporidium* enabled by complete in vitro development in stem cell-
980 derived intestinal epithlium. Cell Host Microbe. 2019;doi.org/10.2139/ssrn.3331307.
981 75. Xu R, Beatty WL, Greigert V, Witola WH, Sibley LD. Multiple pathways for glucose
982 phosphate transport and utilization support growth of Cryptosporidium parvum. bioRxiv.
983 2023. Epub 2023/07/10. doi: 10.1101/2023.06.27.546703. PubMed PMID: 37425855;
984 PubMed Central PMCID: PMCPMC10327089.
985 76. Akey ME, Xu R, Ravindran S, Funkhouser-Jones L, Sibley LD. Apical Secretory
986 Glycoprotein Complex Contributes to Cell Attachment and Entry by Cryptosporidium
987 parvum. mBio. 2023;14(1):e0306422. Epub 2023/02/02. doi: 10.1128/mbio.03064-22.
988 PubMed PMID: 36722968; PubMed Central PMCID: PMCPMC9973360.
989 77. Xu R, Feng Y, Xiao L, Sibley LD. Insulinase-like Protease 1 Contributes to Macrogamont
990 Formation in Cryptosporidium parvum. mBio. 2021;12(2). Epub 2021/03/11. doi:
991 10.1128/mBio.03405-20. PubMed PMID: 33688009; PubMed Central PMCID:
992 PMCPMC8092296.
993 78. Kuhlenschmidt TB, Rutaganira FU, Long S, Tang K, Shokat KM, Kuhlenschmidt MS, et al.
994 Inhibition of Calcium-Dependent Protein Kinase 1 (CDPK1) In Vitro by
995 Pyrazolopyrimidine Derivatives Does Not Correlate with Sensitivity of Cryptosporidium
996 parvum Growth in Cell Culture. Antimicrob Agents Chemother. 2015;60(1):570-9.
997 79. Current WL. Techniques and laboratory maintenance of *Cryptosporidium*. In: Dubey JP,
998 Speer CA, Fayer R, editors. Cryptosporidiosis of Man and Animals. Boca Raton, FL: CRC
999 Press; 1990. p. 44-77.
1000 80. Mehta S, Sibley LD. Actin depolymerizing factor controls actin turnover and gliding motility
1001 in Toxoplasma gondii. Mol Biol Cell. 2011;22(8):1290-9. Epub 20110223. doi:
1002 10.1091/mbc.E10-12-0939. PubMed PMID: 21346192; PubMed Central PMCID:
1003 PMCPMC3078074.
1004 81. Behnke MS, Radke JB, Smith AT, Sullivan WJ, Jr., White MW. The transcription of
1005 bradyzoite genes in Toxoplasma gondii is controlled by autonomous promoter elements.
1006 Mol Microbiol. 2008;68(6):1502-18. Epub 20080421. doi: 10.1111/j.1365-
1007 2958.2008.06249.x. PubMed PMID: 18433450; PubMed Central PMCID:
1008 PMCPMC2440561.
1009 82. Waldman BS, Schwarz D, Wadsworth MH, 2nd, Saeij JP, Shalek AK, Lourido S.
1010 Identification of a Master Regulator of Differentiation in Toxoplasma. Cell.
1011 2020;180(2):359-72 e16. Epub 20200116. doi: 10.1016/j.cell.2019.12.013. PubMed
1012 PMID: 31955846; PubMed Central PMCID: PMCPMC6978799.
1013 83. Huang W, Tang K, Chen C, Arrowood MJ, Chen M, Guo Y, et al. Sequence introgression
1014 from exogenous lineages underlies genomic and biological differences among
1015 Cryptosporidium parvum IOWA lines. Water Res. 2024;254:121333. Epub 20240217.
1016 doi: 10.1016/j.watres.2024.121333. PubMed PMID: 38402753; PubMed Central PMCID:
1017 PMCPMC10994760.
1018

1019

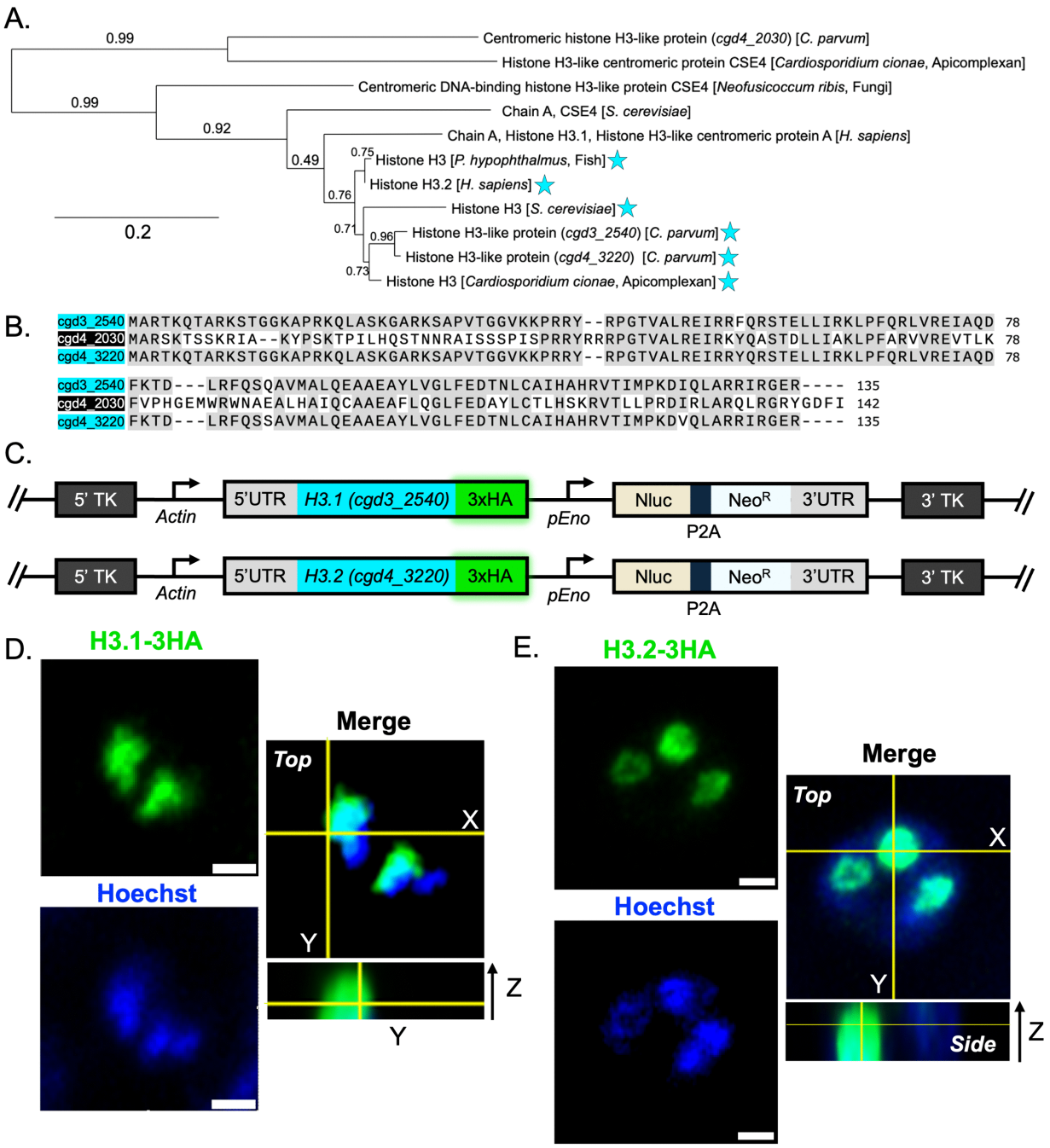

Figure 1: Characterization of centromeric histone H3 (CENH3) and histone H3 candidates in *C. parvum* and construction of Histone H3-3HA tagged strains. (A) Phylogenetic relationship of *C. parvum* H3 and centromeric H3 (CENH3) histones and their corresponding top BLASTP hits in other eukaryotes, apicomplexan parasites, *Saccharomyces cerevisiae*, or *Homo sapiens*. Cyan stars represent annotated histone H3 genes. (B) Protein sequence alignment of H3

1026 (cyan) and CENH3 (black) in *C. parvum*. Amino acids that are identical between at least two
1027 sequences are highlighted in grey. (C) Diagram of the targeting constructs designed to replace
1028 the endogenous *tk* locus with a second copy of either of the genes annotated as Histone H3-like
1029 proteins in *C. parvum* (*cgd3_2540* or *cgd4_3220*), a 3HA tag, and a Nluc-P2A-NeoR cassette.
1030 (D) Immunofluorescence staining of transgenic H3.1-3HA or (E) H3.2-3HA parasites. HCT-8
1031 cells were infected with transgenic oocysts, fixed at 18 hpi, and stained with rat anti-HA
1032 followed by the secondary antibody Alexa Fluor 488 goat anti-rat IgG. Hoechst was used for
1033 nuclear staining. Images were acquired as Z-stacks using a Zeiss LSM-880 Laser Scanning
1034 Confocal microscope equipped with Airyscan (LSCM-A) and are presented with orthogonal
1035 views. Scale bars, 1 μm. Data represent two biological replicates, each with 3-5 technical
1036 replicates.
1037

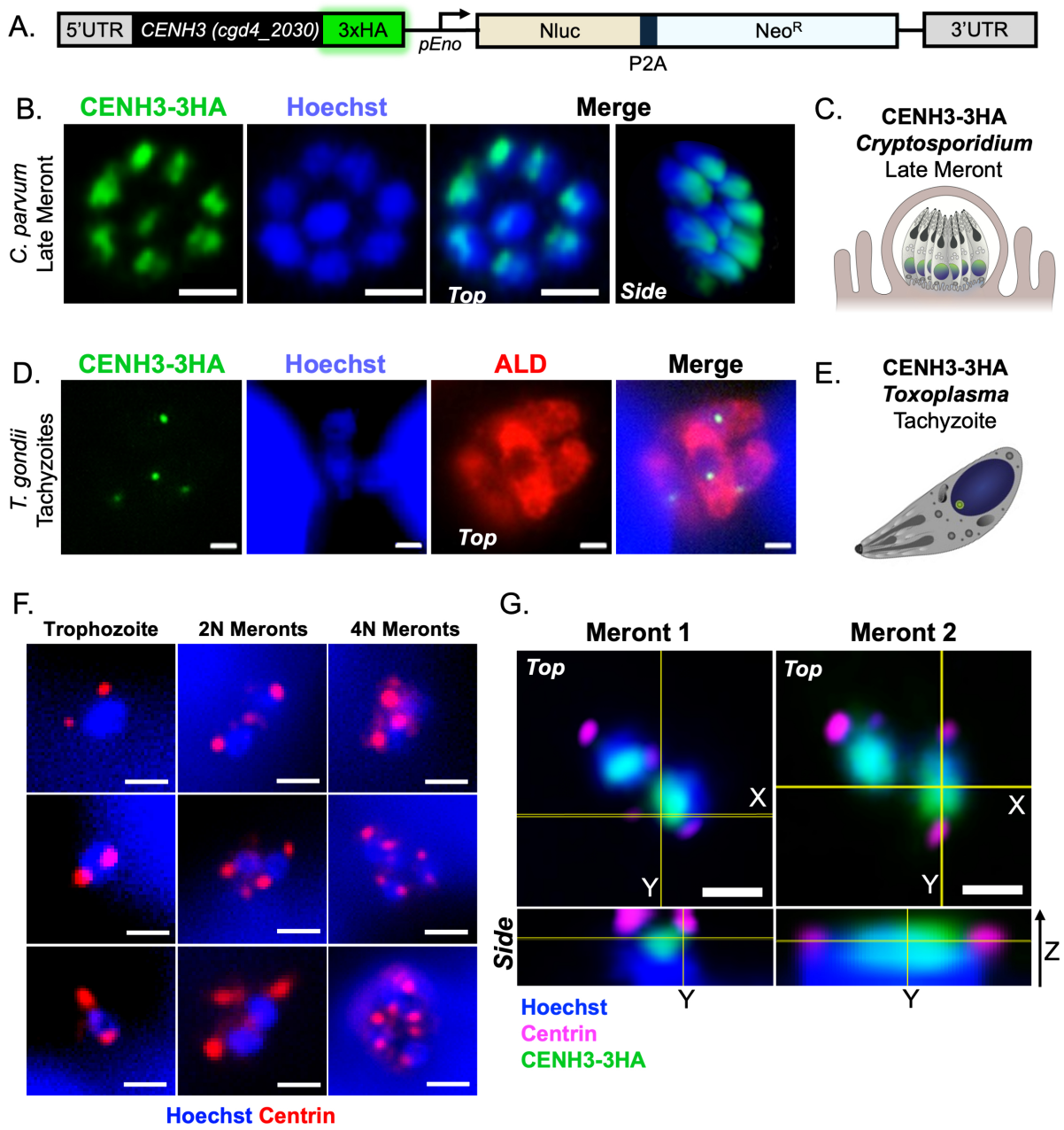

Figure 2. The staining pattern of *C. parvum* centromeric histone H3 (CENH3) is distinct from *Toxoplasma* and remains diffuse during mitosis. (A) Diagram of the targeting construct designed to add a 3HA tag and Nluc-P2A-Neo^R cassette to the C-terminus of the *C. parvum* CENH3 (*cgd4_2030*). (B) HCT-8 cells were infected with CENH3-3HA *C. parvum* parasites, fixed at 22 hpi, and stained with rat anti-HA, followed by the secondary antibody Alexa Fluor 488 goat anti-rat IgG followed by Hoechst staining. Images were acquired as Z-stacks using

1045 LSCM-A and are presented with orthogonal views. Scale bars, 1 µm. (C) Cartoon depiction
1046 corresponding to the microscopy image in panel (B). In *Cryptosporidium*, a late-stage meront
1047 contains eight nuclei that have recently completed cytokinesis to form mature merozoites. The
1048 CENH3-3HA signal within each nucleus displays a diffuse staining pattern in *C. parvum*. (D)
1049 HCT-8 cells were infected with CENH3-3HA *T. gondii* parasites, fixed at 24 hpi, and stained
1050 with rat anti-HA and rabbit anti-aldolase (ALD) to visualize the cytosol, followed by secondary
1051 antibodies Alexa Fluor 488 goat anti-rat IgG and Alexa Fluor 568 anti-rabbit IgG. Hoechst was
1052 used for nuclear staining. Images were acquired as Z-stacks using LSCM-A and are presented
1053 with orthogonal views. Scale bars, 1 µm. (E) Cartoon depiction corresponding to the microscopy
1054 image in panel (D). In *T. gondii* tachyzoites, the CENH3-3HA signal within each nucleus
1055 displays a discrete staining pattern. (F) HCT-8 cells were infected with excysted *C. parvum*
1056 sporozoites for 2 h, then washed twice to remove extracellular parasites. Cultures were fixed at
1057 30 min increments between 6-9 hpi to identify the first (trophozoites with one nucleus), second
1058 (early meronts with 2 nuclei), and third (mid-stage meronts with 4 nuclei) mitotic divisions
1059 during the first round of merogony by widefield microscopy. Scale bars, 1 µm. (G) Cultures were
1060 infected with CENH3-3HA *C. parvum* sporozoites for 2 h, washed, and fixed at 6.5 hpi to
1061 capture the first round of mitosis. Cultures were stained with rat anti-HA, rabbit anti-centrin-1,
1062 followed by secondary antibodies Alexa Fluor 488 goat anti-rat IgG, Alexa Fluor 568 goat anti-
1063 rabbit IgG, and lastly Hoechst. Parasites undergoing mitosis were identified by having two
1064 centrin-1 points per nucleus, whereas parasites in interphase had only one centrin-1 point.
1065 Images were acquired as Z-stacks using LSCM-A and are presented with orthogonal views.
1066 Scale bars, 1 µm. Data represent 2-3 biological replicates, each with 3-5 technical replicates.
1067

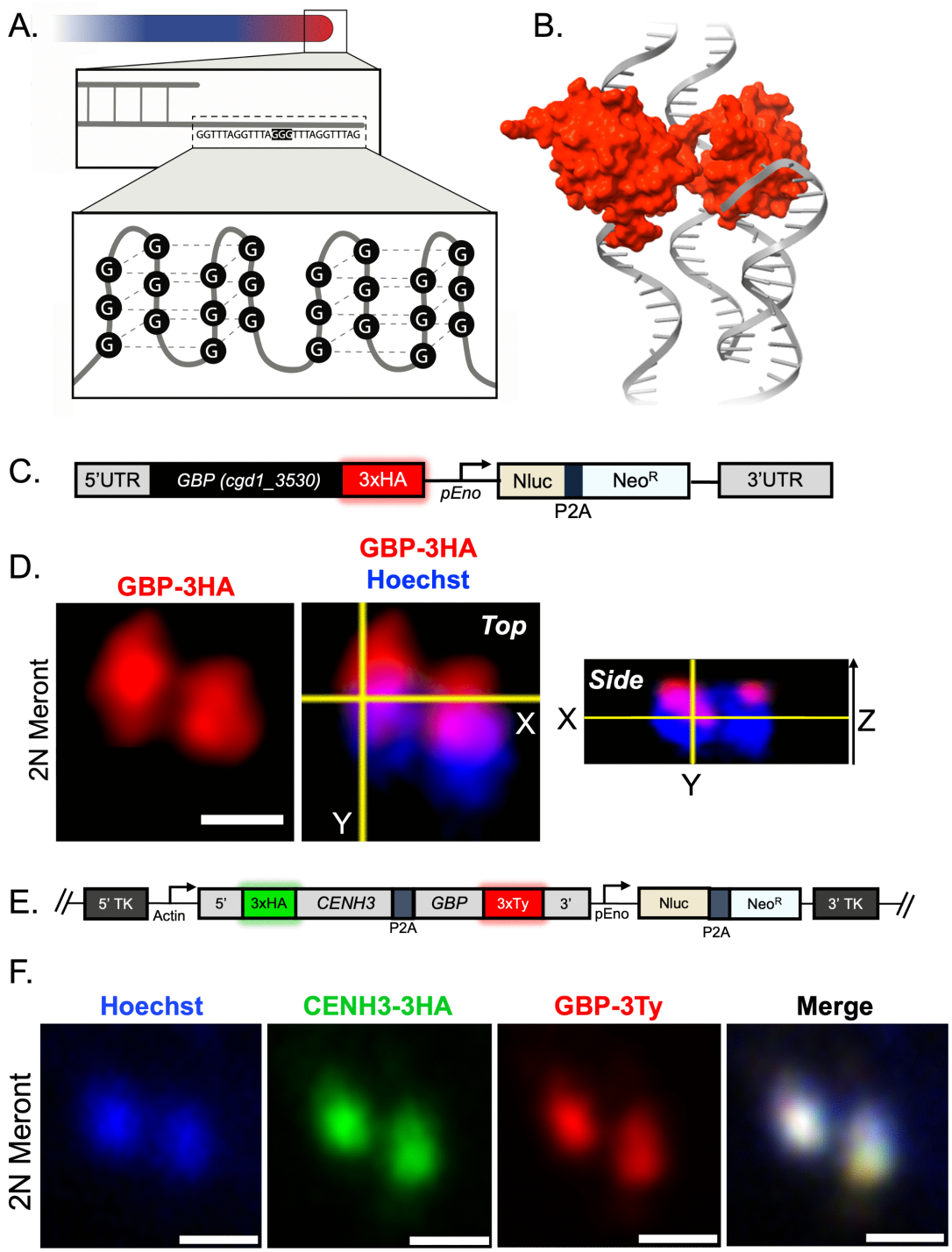

Figure 3: The telomere (G-strand binding protein, GBP) staining pattern is apical in *C. parvum* and overlaps with the centromere (CENH3) staining pattern. (A) The 3' overhang single-stranded DNA at the end of telomeres contains repetitive sequences $(GGTTTA)_n$ in *C. parvum* that form G-quadruplex structures. (B) The G-quadruplex binding protein (GBP) is

1073 essential for forming and stabilizing these structures. The sequence of *Cp*GBP and its binding
1074 motif has been previously determined and the protein structure is modeled by Alphafold and
1075 ChimeraX [51]. (C) Diagram of the targeting construct designed to add a 3HA tag and Nluc-
1076 P2A-Neo^{R} cassette to the C-terminus of the G-quadruplex binding proteins gene *(*GBP*,*
1077 *cgd1_3530)* (D) HCT-8 cells were infected with GBP-3HA parasites, fixed at 6.5 hpi to capture
1078 early meronts (2 nuclei), and stained with rat anti-HA, followed by the secondary antibody Alexa
1079 Fluor 488 goat anti-rat IgG. Hoechst was used for nuclear staining. Images were acquired as Z-
1080 stacks using LSCM-A and are presented with orthogonal views and the scale bar is 1 µm. (E)
1081 Diagram of the targeting construct designed to replace the endogenous *tk* locus with a second
1082 copy of CENH3 N-terminally tagged with 3HA and GBP with a C-terminal 3xTy tag separated
1083 with a P2A split peptide. (F) Immunofluorescence staining of transgenic 3HA-CENH3-GBP-3Ty
1084 parasites. HCT-8 cells were infected with transgenic oocysts, fixed at 6.5 hpi to capture early
1085 meronts (2 nuclei), and stained with rat anti-HA and mouse anti-Ty, followed by a secondary
1086 antibody stain containing Alexa Fluor 488 goat anti-rat IgG and Alexa Fluor 568 goat-anti
1087 mouse. Hoechst was used for nuclear staining. Images were acquired as Z-stacks using LSCM-A
1088 and are presented with orthogonal views. Scale bars, 1 µm. Data represent 2-3 biological
1089 replicates, each with 3-5 technical replicates.
1090

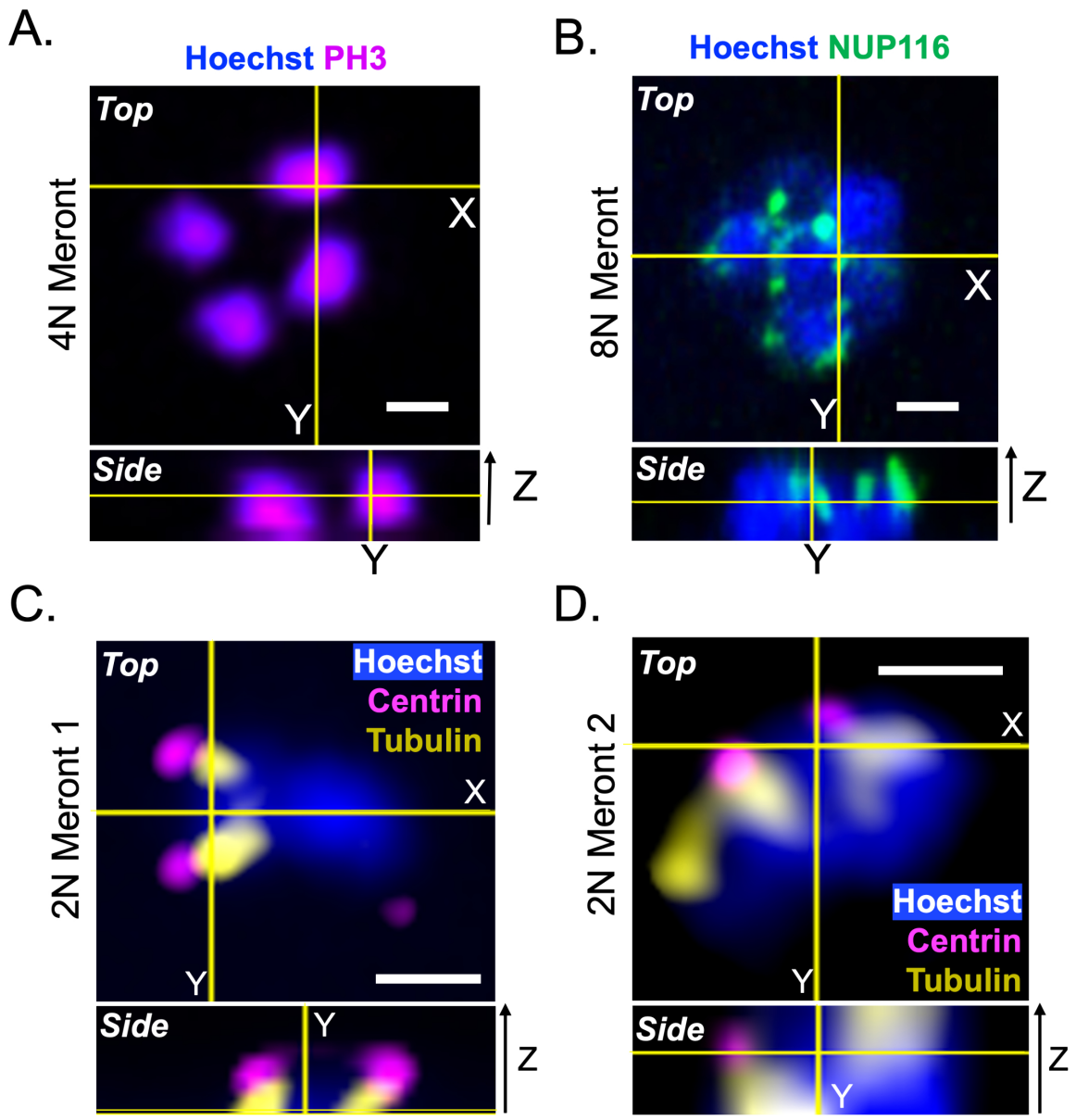

Figure 4: Mitotically active DNA, microtubules, and the nuclear pore proteins as visualized by antibody staining in *C. parvum*. (A) HCT-8 cells were infected with wild type parasites, fixed at 18 hpi, and stained with rabbit anti-phosphorylated Histone H3 (PH3) followed by an Alexa Fluor 568 goat anti-rabbit IgG antibody. DNA was stained with Hoechst and a mid-stage meront with 4 nuclei is shown. (B) Parasites were prepared identically to panel A, but were stained with a rabbit polyclonal antibody that recognizes a subunit of the nuclear pore in *Plasmodium falciparum* (NUP116) followed by an Alexa Fluor 568 goat anti-rabbit IgG

1099 antibody and Hoechst. A late-stage meronts with 8 nuclei is shown. (C, D) HCT-8 cells were
1100 infected with wild-type parasites, fixed at 6.5 hpi to capture early meronts (2 nuclei), and stained
1101 with rabbit anti-centrin-1 and mouse anti-tubulin, followed by the secondary antibodies Alexa
1102 Fluor 488 goat anti-mouse IgG, Alexa Fluor 568 goat anti-rabbit IgG, and Hoechst. The nucleus
1103 in the first meront (C) may be an example of early mitosis, whereas the second meront (D) may
1104 be an example of a later phase of the mitotic process. Images were acquired as Z-stacks using
1105 LSCM-A and are presented with orthogonal views. Scale bars, 1 μm. Data represent two
1106 biological replicates, each with 2-5 technical replicates.
1107

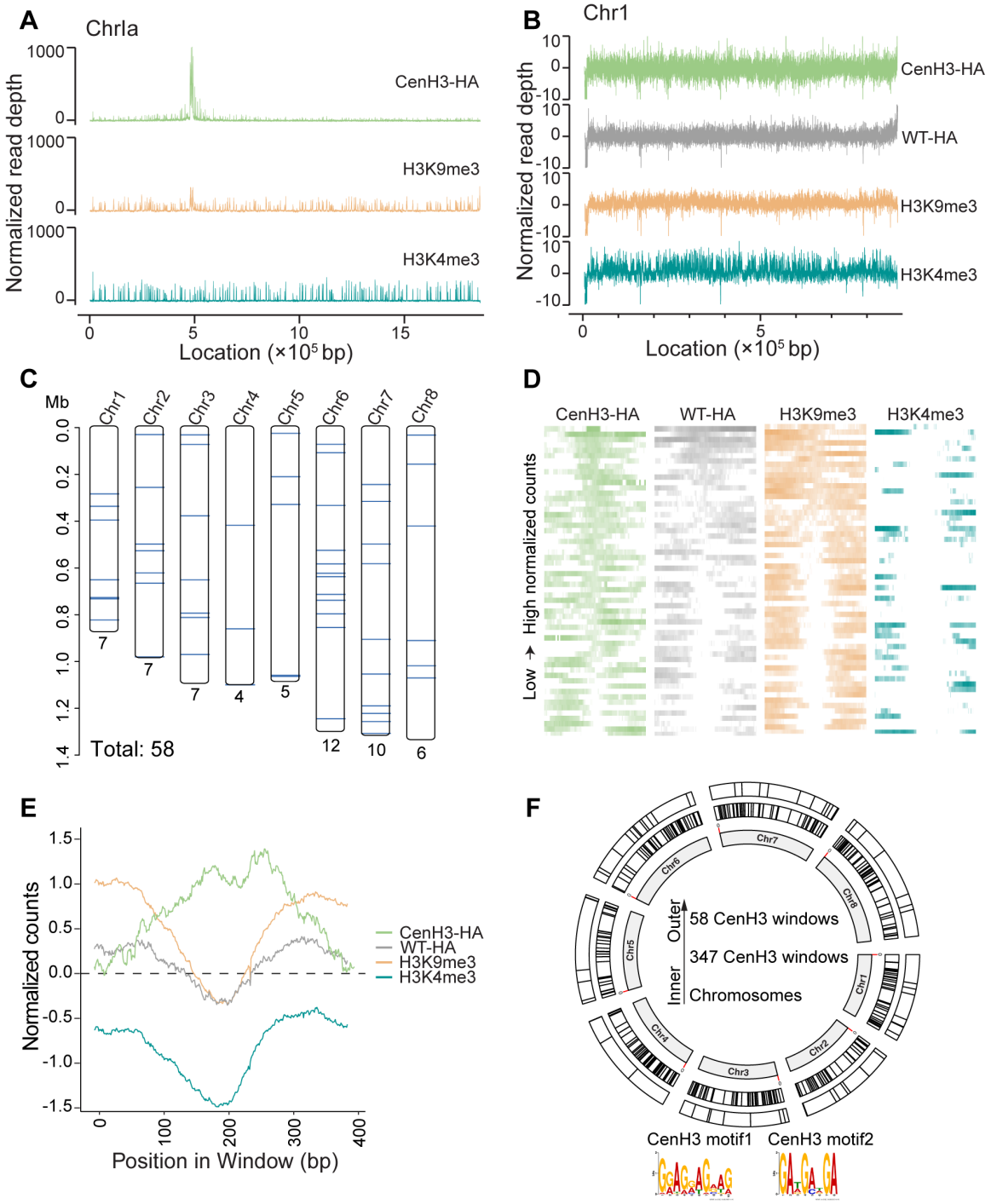

Figure 5. Genome-wide distribution of CENH3 in *Toxoplasma gondii* and *Cryptosporidium parvum*. (A) Genome browser view of *T. gondii* chromosome Ia showing CUT&RUN signals for CENH3-HA (HA antibody), H3K9me3, and H3K4me3. CENH3 signal enrichment positively correlates with H3K9me3 and inversely with H3K4me3. Peaks of CENH3 enrichment are

1113 indicated (red arrows). (B) Genome browser view of *C. parvum* chromosome I, showing
1114 CUT&RUN signals for CENH3-HA *C. parvum* captured with HA antibody and wild type *C.*
1115 *parvum* captured with HA antibody (referred to as WT-HA), H3K9me3, and H3K4me3
1116 (captured with antibodies). (C) Chromosomal distribution of the 58 CENH3-enriched windows
1117 in intergenic regions of *C. parvum* chromosomes (Chr#). Numbers below each chromosome
1118 indicate the number of windows. (D) Heatmaps of CUT&RUN signals for the groups shown in
1119 (B) within a 400 bp window around all 58 CENH3-enriched windows . Each row represents an
1120 individual centromeric site, ranked by signal intensity. (E) Average signal profiles for CENH3-
1121 HA (green), WT-HA (gray), H3K9me3 (orange), and H3K4me3 (teal) across the 400 bp window
1122 around CENH3 sites. (F) Circos plot of CENH3-associated motifs. From inner to outer rings:
1123 chromosomes, locations of 347 CENH3-enriched windows found in coding regions (black), and
1124 locations of 58 CENH3-enriched windows found in intergenic regions (black). Representative
1125 sequence logos for motif 1 and motif 2 are shown.
1126
1127

1128

1129 **Supporting Information**

1130 **S1 Fig.** Tagged versions of the H3.1, H3.2, and CENH3 and GBP genes were inserted into the tk
1131 locus in *Cryptosporidium parvum*.
1132 **S2 Fig.** The GBP and CENH3 expression overlaps in *Cryptosporidium parvum.*
1133 **S3 Fig.** The GBP and CENH3 gene were successfully tagged with HA tag and/or a spaghetti
1134 monster HA tag in C*ryptosporidium parvum*.
1135 **S4 Fig.** Additional images of centrin and tubulin staining in *Cryptosporidium parvum.*
1136 **S5 Fig.** Genome-wide distribution of CENH3 in *Toxoplasma gondii*.
1137 **S6 Fig.** Genome-wide distribution of CENH3 in *Cryptosporidium parvum*.
1138

1139 **S1 Table.** Transgenic *Cryptosporidium* strains used in this study.
1140 **S2 Table.** Key Resources used in the experiments.
1141 **S3 Table.** Oligonucleotides and plasmids used in this study.
1142

1143 **S1 Dataset** Information of sequencing samples from the Cut&Run and summary statistics of the
1144 data.
1145 **S2 Dataset** Genomic location of the CENH3 sites within coding regions.
1146 **S3 Dataset** Genomic location of the CENH3 sites within intergenic regions.
1147